Journal of Computational Physics 375 (2018) 659–683

Contents lists available at ScienceDirect

Journal of Computational Physics

www.elsevier.com/locate/jcp

A new type of multi-resolution WENO schemes with increasingly higher order of accuracy

Jun Zhu [a,1], Chi-Wang Shu [b,*,2]

[a] College of Science, Nanjing University of Aeronautics and Astronautics, Nanjing, Jiangsu 210016, PR China
[b] Division of Applied Mathematics, Brown University, Providence, RI 02912, USA

ARTICLE INFO

Article history:
Received 16 July 2018
Received in revised form 2 September 2018
Accepted 4 September 2018
Available online 6 September 2018

Keywords:
Multi-resolution scheme
Weighted essentially non-oscillatory scheme
Hyperbolic conservation laws
Finite difference
Finite volume

ABSTRACT

In this paper, a new type of high-order finite difference and finite volume multi-resolution weighted essentially non-oscillatory (WENO) schemes is presented for solving hyperbolic conservation laws. We only use the information defined on a hierarchy of nested central spatial stencils and do not introduce any equivalent multi-resolution representation. These new WENO schemes use the same large stencils as the classical WENO schemes in [25,45], could obtain the optimal order of accuracy in smooth regions, and could simultaneously suppress spurious oscillations near discontinuities. The linear weights of such WENO schemes can be any positive numbers on the condition that their sum equals one. This is the first time that a series of unequal-sized hierarchical central spatial stencils are used in designing high-order finite difference and finite volume WENO schemes. These new WENO schemes are simple to construct and can be easily implemented to arbitrary high order of accuracy and in higher dimensions. Benchmark examples are given to demonstrate the robustness and good performance of these new WENO schemes.

1. Introduction

In this paper, we propose a new type of finite difference and finite volume multi-resolution weighted essentially non-oscillatory (WENO) schemes for solving the hyperbolic conservation laws

$$\begin{cases} u_t + \nabla \cdot f(u) = 0, \\ u(x_1, ..., x_n, 0) = u_0(x_1, ..., x_n). \end{cases} \tag{1.1}$$

Let us start by mentioning a few features and advantages of these new WENO schemes. The first is that the linear weights can be any positive numbers on the condition that their sum is one. The second is their simplicity and easy extension to multi-dimensions. The third is that a multi-resolution style hierarchy of nested central spatial stencils is used in the WENO spatial reconstructions, different from the existing WENO schemes. The last is that the number of spatial stencils is no bigger than that of the same order accurate classical finite difference or finite volume WENO schemes in [25,45].

* Corresponding author.
E-mail addresses: zhujun@nuaa.edu.cn (J. Zhu), shu@dam.brown.edu (C.-W. Shu).
[1] Research was supported by NSFC grant 11872210.
[2] Research was supported by ARO grant W911NF-15-1-0226 and NSF grant DMS-1719410.

https://doi.org/10.1016/j.jcp.2018.09.003
0021-9991/

Let us review briefly the history of essentially non-oscillatory (ENO) and WENO schemes. In 1985, Harten et al. [22] proposed a weaker version of the total variation diminishing (TVD) criterion [14] and then established a basis for the reconstruction of high-order ENO type schemes. In 1987, Harten et al. [21] proposed a series of finite volume ENO schemes to solve one-dimensional problems. The important objective of such ENO schemes was to apply the smoothest candidate stencil among all central and biased spatial stencils to get high order approximation of the variables at the cell boundaries to keep optimal accuracy in smooth regions and to avoid spurious oscillations near isolated discontinuities. See also [46,47] for the finite difference ENO schemes, which are more efficient for multi-dimensional computation. In 1994, Liu et al. [30] designed the first WENO scheme which did not use the optimal smooth candidate stencil but applied a linear convex combination of all candidate spatial stencils. Thereafter, Jiang and Shu [25] improved such WENO scheme to higher order of accuracy on the same stencils, and proposed general smoothness indicators and nonlinear weights. Subsequently, the optimized WENO schemes [48], monotonicity preserving WENO schemes [2], hybrid compact WENO schemes [38,41], robust WENO schemes [23,37,42], a hierarchical reconstruction (HR) method [31–36,51,52] for limiting numerical solutions of the discontinuous Galerkin, finite difference and finite volume schemes, and central/compact WENO (CWENO) schemes [1,5,10,13,26,28,29,40] were also developed with various advantages. The different types of ENO and WENO schemes [6,7,15,24,25,30,43,46,47,57,58] have been quite successful in numerical simulations for different problems in applications containing strong discontinuities and sophisticated smooth structures.

As it is well known, the multi-resolution method was designed for the sake of reducing the computing costs of high resolution schemes. The solution of hyperbolic conservation laws might contain strong discontinuities in small and isolated regions and might be smooth in the remaining regions which form the majority part of the computational domain, hence the multi-resolution technique could focus its effort in the regions which contain strong discontinuities. The original idea about this type of multi-resolution method was proposed by Harten [16–20] for solving the hyperbolic equations. Then Dahmen et al. [11] analyzed the multi-resolution methods for the conservation laws. Chiavassa et al. [9] studied the multi-resolution-based adaptive schemes for the hyperbolic conservation laws. In 2007, Bürger et al. [4] proposed a fifth order WENO scheme together with a multi-resolution technique to solve for multi-species kinematic flow models. Roughly speaking, the objective of applying the multi-resolution technique is to focus the computational effort mainly in the small regions containing strong discontinuities.

In this paper, we first design a new type of finite difference WENO schemes borrowing the original idea of the multi-resolution methods [16–20] using the information defined on one one-point central stencil and one three-point central stencil to obtain a third-order approximation at the boundary points of the target cell in smooth regions, and when there is a discontinuity in the three-point central stencil, the information of the three-point stencil is effectively abandoned (through a small nonlinear weight assigned to it) and the approximation order degrades to one. If the solution is smooth enough, the information defined on such two central spatial stencils and one five-point central stencil is used to obtain a fifth-order approximation at the cell boundary points. Then based on the same assumption, the information of such three central spatial stencils together with one seventh-point central stencil is used to obtain a seventh-order approximation, and this methodology could be used to design a ninth-order and any arbitrary higher order approximations on the condition that there are no discontinuities inside the biggest central spatial stencil. To do so, we only use the point values of the numerical solution on a hierarchy of nested central spatial stencils, and do not introduce any equivalent multi-resolution representations in the finite difference framework, which is easily extended to the finite volume framework as well. The formulations of such high-order approximations which reveal the relationship between reconstructed polynomials of different degrees at cell boundary points are designed in the classical WENO spatial reconstruction fashion [25,45]. After performing such WENO spatial reconstruction procedures and then applying a third-order TVD Runge–Kutta time discretization [46], we could get a new type of arbitrary high-order finite difference and finite volume WENO schemes. In the construction of these new WENO schemes, the positive linear weights can be arbitrarily chosen as long as they sum to one. Since the information of the hierarchical central stencils is used to construct polynomials for sustaining high-order approximations at the boundary points, the degrading of accuracy near discontinuities is gradual, in the sense that the accuracy reduces to first-order if the three-point central stencil contains a discontinuity, the accuracy reduces to third-order if the solution is smooth in the three-point central stencil but not in the five-point central stencil, the accuracy reduces to fifth-order if the solution is smooth in the five-point central stencil but not in the seventh-point central stencil, and so on. Moreover, the number of the unequal-sized central spatial stencils does not exceed that of the same order classical WENO schemes in [25,45].

The organization of the paper is as follows. In Section 2, we construct the new finite difference and finite volume multi-resolution WENO schemes in detail. In Section 3, benchmark numerical examples are provided to demonstrate the numerical accuracy and resolution of this new type of arbitrary high-order WENO schemes. Concluding remarks are given in Section 4.

2. Multi-resolution WENO schemes

The detailed flowchart of the new high-order finite difference and finite volume multi-resolution WENO schemes from the third-order to ninth-order is described as follows.

2.1. Finite difference multi-resolution WENO schemes

We first consider one-dimensional hyperbolic conservation laws

$$\begin{cases} u_t + f_x(u) = 0, \\ u(x,0) = u_0(x), \end{cases} \tag{2.1}$$

and approximate the first equation of (2.1) as

$$\frac{du}{dt} = L(u) \approx -f_x(u). \tag{2.2}$$

For simplicity, we consider a uniform mesh x_i with the uniform mesh size $h = x_{i+1} - x_i$. We denote the half point as $x_{i+1/2} = \frac{1}{2}(x_i + x_{i+1})$. $u_i(t)$ is the numerical approximation to the nodal point value $u(x_i, t)$ of the exact solution. The right hand side of (2.2) is given by a conservative approximation as

$$\frac{du_i(t)}{dt} = L(u)_i = -\frac{1}{h}(\hat{f}_{i+1/2} - \hat{f}_{i-1/2}), \tag{2.3}$$

in which $\hat{f}_{i+1/2}$ is the numerical flux which can be a third-order, fifth-order, seventh-order, or ninth-order approximation, to ensure $\frac{1}{h}(\hat{f}_{i+1/2} - \hat{f}_{i-1/2})$ is the same order approximation to $f_x(u)$ at $x = x_i$, as described in detail in [47]. In order to ensure correct upwind biasing and stability, we split the flux $f(u)$ into $f(u) = f^+(u) + f^-(u)$ with $\frac{df^+(u)}{du} \geq 0$ and $\frac{df^-(u)}{du} \leq 0$, and then approximate each of them separately using its own wind direction. A simple Lax–Friedrichs splitting $f^{\pm}(u) = \frac{1}{2}(f(u) \pm \alpha u)$ is used in this paper, in which α is set as $\max_u |f'(u)|$ over the whole range of u. Thus the numerical flux is split accordingly

$$\hat{f}_{i+1/2} = \hat{f}^+_{i+1/2} + \hat{f}^-_{i+1/2}. \tag{2.4}$$

All the one-dimensional and two-dimensional finite difference and finite volume WENO schemes are based on the simple reconstruction procedure detailed below. Suppose we are given the cell averages $\bar{w}_j = \frac{1}{h}\int_{x_j-h/2}^{x_j+h/2} w(x)dx$ for all j and would like to obtain an associated order WENO polynomial approximation $w_i(x)$ defined on $I_i = [x_{i-1/2}, x_{i+1/2}]$, based on upwind-biased stencils consisting of $I_j = [x_{j-1/2}, x_{j+1/2}]$ with $j = i-\ell, ..., i+\ell$ for $\ell = 0, ..., 5$, respectively. The procedure is summarized as follows.

Reconstruction Algorithm.

Step 1. Select a series of central spatial stencils and reconstruct different degree polynomials.

Step 1.1. For a third-order spatial approximation, we choose two central spatial stencils $T_1 = \{I_i\}$ and $T_2 = \{I_{i-1}, I_i, I_{i+1}\}$. It is easy to reconstruct a zeroth degree polynomial $q_1(x)$ and a quadratic polynomial $q_2(x)$ which satisfy

$$\frac{1}{h}\int_{x_j-h/2}^{x_j+h/2} q_1(x)dx = \bar{w}_j, \ \ j = i, \tag{2.5}$$

and

$$\frac{1}{h}\int_{x_j-h/2}^{x_j+h/2} q_2(x)dx = \bar{w}_j, \ \ j = i-1, i, i+1. \tag{2.6}$$

Step 1.2. For a fifth-order spatial approximation, we use a central spatial stencil $T_3 = \{I_{i-2}, ..., I_{i+2}\}$. It is easy to reconstruct a quartic polynomial $q_3(x)$ which satisfies

$$\frac{1}{h}\int_{x_j-h/2}^{x_j+h/2} q_3(x)dx = \bar{w}_j, \ \ j = i-2, ..., i+2. \tag{2.7}$$

Step 1.3. For a seventh-order spatial approximation, we use a central spatial stencil $T_4 = \{I_{i-3}, ..., I_{i+3}\}$. It is easy to reconstruct a sixth degree polynomial $q_4(x)$ which satisfies

$$\frac{1}{h}\int_{x_j-h/2}^{x_j+h/2} q_4(x)dx = \bar{w}_j, \ \ j = i-3, ..., i+3. \tag{2.8}$$

Step 1.4. For a ninth-order spatial approximation, we use a central spatial stencil $T_5 = \{I_{i-4}, ..., I_{i+4}\}$. Then an eighth degree polynomial $q_5(x)$ is obtained as

$$\frac{1}{h}\int_{x_j-h/2}^{x_j+h/2} q_5(x)dx = \bar{w}_j, \ \ j = i-4, ..., i+4. \tag{2.9}$$

The explicit expressions of these reconstruction polynomials are given in [44] and we omit them here.

Step 2. Obtain equivalent expressions for these reconstruction polynomials of different degrees. To keep consistent notation, we will denote $p_1(x) = q_1(x)$ and obtain

$$p_{\ell_2}(x) = \frac{1}{\gamma_{\ell_2,\ell_2}} q_{\ell_2}(x) - \sum_{\ell=1}^{\ell_2-1} \frac{\gamma_{\ell,\ell_2}}{\gamma_{\ell_2,\ell_2}} p_\ell(x), \tag{2.10}$$

with $\sum_{\ell=1}^{\ell_2} \gamma_{\ell,\ell_2} = 1$ and $\gamma_{\ell_2,\ell_2} \neq 0$ for $\ell_2 = 2, 3, 4, 5$. We explain them in detail as follows.

Step 2.1. For the third-order approximation, with similar ideas for CWENO schemes in earlier references [5,28,29] as well, a polynomial $p_2(x)$ is defined through

$$p_2(x) = \frac{1}{\gamma_{2,2}} q_2(x) - \frac{\gamma_{1,2}}{\gamma_{2,2}} p_1(x), \tag{2.11}$$

with $\gamma_{1,2} + \gamma_{2,2} = 1$ and $\gamma_{2,2} \neq 0$.

Step 2.2. For the fifth-order approximation, a polynomial $p_3(x)$ is defined through

$$p_3(x) = \frac{1}{\gamma_{3,3}} q_3(x) - \frac{\gamma_{1,3}}{\gamma_{3,3}} p_1(x) - \frac{\gamma_{2,3}}{\gamma_{3,3}} p_2(x), \tag{2.12}$$

with $\sum_{\ell=1}^{3} \gamma_{\ell,3} = 1$ and $\gamma_{3,3} \neq 0$.

Step 2.3. For the seventh-order approximation, a polynomial $p_4(x)$ is defined through

$$p_4(x) = \frac{1}{\gamma_{4,4}} q_4(x) - \sum_{\ell=1}^{3} \frac{\gamma_{\ell,4}}{\gamma_{4,4}} p_\ell(x), \tag{2.13}$$

with $\sum_{\ell=1}^{4} \gamma_{\ell,4} = 1$ and $\gamma_{4,4} \neq 0$.

Step 2.4. For the ninth-order approximation, a polynomial $p_5(x)$ is defined through

$$p_5(x) = \frac{1}{\gamma_{5,5}} q_5(x) - \sum_{\ell=1}^{4} \frac{\gamma_{\ell,5}}{\gamma_{5,5}} p_\ell(x), \tag{2.14}$$

with $\sum_{\ell=1}^{5} \gamma_{\ell,5} = 1$ and $\gamma_{5,5} \neq 0$.

In these expressions, γ_{ℓ,ℓ_2} for $\ell = 1, ..., \ell_2$ and $\ell_2 = 2, 3, 4, 5$ are the linear weights, respectively. Based on a balance between the sharp and essentially non-oscillatory shock transitions in nonsmooth regions and accuracy in smooth regions, following the practice in [12,59–62], we set the linear weights as $\gamma_{\ell,\ell_2} = \frac{\bar{\gamma}_{\ell,\ell_2}}{\sum_{l=1}^{\ell_2} \bar{\gamma}_{l,\ell_2}}$, in which $\bar{\gamma}_{\ell,\ell_2} = 10^{\ell-1}$ for $\ell = 1, ..., \ell_2$ and $\ell_2 = 2, 3, 4, 5$. For example, we take $\bar{\gamma}_{1,2} = 1$ and $\bar{\gamma}_{2,2} = 10$ for the third-order approximation; $\bar{\gamma}_{1,3} = 1$, $\bar{\gamma}_{2,3} = 10$, and $\bar{\gamma}_{3,3} = 100$ for the fifth-order approximation; $\bar{\gamma}_{1,4} = 1$, $\bar{\gamma}_{2,4} = 10$, $\bar{\gamma}_{3,4} = 100$, and $\bar{\gamma}_{4,4} = 1000$ for the seventh-order approximation; $\bar{\gamma}_{1,5} = 1$, $\bar{\gamma}_{2,5} = 10$, $\bar{\gamma}_{3,5} = 100$, $\bar{\gamma}_{4,5} = 1000$, and $\bar{\gamma}_{5,5} = 10000$ for the ninth-order approximation.

Step 3. Compute the smoothness indicators β_{ℓ_2}, which measure how smooth the functions $p_{\ell_2}(x)$ for $\ell_2 = 2, 3, 4, 5$ are in the interval $[x_{i-1/2}, x_{i+1/2}]$. We use the same recipe for the smoothness indicators as in [25,45]:

$$\beta_{\ell_2} = \sum_{\alpha=1}^{\kappa} \int_{x_i-h/2}^{x_i+h/2} h^{2\alpha-1} \left(\frac{d^\alpha p_{\ell_2}(x)}{dx^\alpha}\right)^2 dx, \quad \ell_2 = 2, 3, 4, 5, \tag{2.15}$$

where $\kappa = 2(\ell_2 - 1)$ for $\ell_2 = 2, 3, 4, 5$, respectively. The only exception is β_1, which we magnify from zero to a value defined below. We first denote

$$\varsigma_0 = (\bar{w}_i - \bar{w}_{i-1})^2, \quad \varsigma_1 = (\bar{w}_{i+1} - \bar{w}_i)^2, \tag{2.16}$$

$$\bar{\gamma}_{0,1} = \begin{cases} 1, & \varsigma_0 \geq \varsigma_1, \\ 10, & \text{otherwise}, \end{cases} \quad \bar{\gamma}_{1,1} = 11 - \bar{\gamma}_{0,1}, \tag{2.17}$$

$$\gamma_{0,1} = \frac{\bar{\gamma}_{0,1}}{\bar{\gamma}_{0,1} + \bar{\gamma}_{1,1}}, \quad \gamma_{1,1} = 1 - \gamma_{0,1}, \tag{2.18}$$

$$\sigma_0 = \gamma_{0,1}\left(1 + \frac{|\varsigma_0 - \varsigma_1|^\kappa}{\varsigma_0 + \varepsilon}\right), \quad \sigma_1 = \gamma_{1,1}\left(1 + \frac{|\varsigma_0 - \varsigma_1|^\kappa}{\varsigma_1 + \varepsilon}\right), \quad \sigma = \sigma_0 + \sigma_1, \tag{2.19}$$

in which $\kappa = 1, 2, 3, 4$ (for the third-order, fifth-order, seventh-order, and ninth-order approximations, respectively), ε is a small positive number to avoid the denominator of (2.19) to become zero and will be addressed later. Then we set

$$\beta_1 = \frac{1}{\sigma^2}\left(\sigma_0(\bar{w}_i - \bar{w}_{i-1}) + \sigma_1(\bar{w}_{i+1} - \bar{w}_i)\right)^2. \tag{2.20}$$

Step 4. Compute the nonlinear weights based on the linear weights and the smoothness indicators. We adopt the WENO-Z recipe as shown in [3,8], with τ_{ℓ_2} for $\ell_2 = 2, 3, 4, 5$ defined as related to the absolute deference between the smoothness indicators:

$$\tau_{\ell_2} = \left(\frac{\sum_{\ell=1}^{\ell_2 - 1} |\beta_{\ell_2} - \beta_\ell|}{\ell_2 - 1}\right)^{\ell_2 - 1}, \quad \ell_2 = 2, 3, 4, 5. \tag{2.21}$$

The nonlinear weights are then given as

$$\omega_{\ell_1,\ell_2} = \frac{\bar{\omega}_{\ell_1,\ell_2}}{\sum_{\ell=1}^{\ell_2} \bar{\omega}_{\ell,\ell_2}}, \quad \bar{\omega}_{\ell_1,\ell_2} = \gamma_{\ell_1,\ell_2}\left(1 + \frac{\tau_{\ell_2}}{\varepsilon + \beta_{\ell_1}}\right), \ \ell_1 = 1, ..., \ell_2; \ \ell_2 = 2, 3, 4, 5. \tag{2.22}$$

Here ε is taken as 10^{-10} in all the simulations.

Step 5. The new final reconstruction polynomial $w_i(x)$ is given by

$$w_i(x) = \sum_{\ell=1}^{\ell_2} \omega_{\ell,\ell_2} p_\ell(x), \quad \ell_2 = 2, 3, 4, 5, \tag{2.23}$$

for the third-order, fifth-order, seventh-order, or ninth-order approximations, respectively.

Remark 1. In Step 2 above, the choice of $\bar{\gamma}_{\ell,\ell_2}$ is not unique. For example, we could also take $\bar{\gamma}_{\ell,\ell_2} = 1$ for all $\ell = 1, ..., \ell_2$. Our numerical experiments indicate that such different choices of the linear weights do not change the optimal order of accuracy in smooth regions, yet bigger linear weights for higher-degree polynomials on bigger central spatial stencils can yield sharper shock transitions near strong discontinuities.

Remark 2. In Step 3 above, the strategy to choose β_1 is different from that for other β_ℓ's. If we use (2.15) to compute β_1, it would equal 0. This does not seem to cause any problems in the accuracy test, the designed high order accuracy can be achieved. However, it does lead to more smeared shock transitions when computing problems containing strong shocks or contact discontinuities. Therefore, we would like to increase the size of β_1 slightly, associated to the smoothness in $\{I_{i-1}, I_i\}$ and in $\{I_i, I_{i+1}\}$, measured by $(\bar{w}_i - \bar{w}_{i-1})^2$ and $(\bar{w}_{i+1} - \bar{w}_i))^2$, with more emphasis on the smaller one of these two measures. The choice of β_1 in (2.20) represents this idea and works well in our numerical experiments.

Remark 3. In Step 4 above, through a Taylor expansion analysis, we can verify that $\beta_{\ell_2} = D(1 + O(h^{r-1}))$ for $\ell_2 = 2, 3, 4, 5$ with $r = 3, 5, 7, 9$, respectively, where D is some non-zero quantity independent of ℓ_2 [25]. It is easy to verify that $\beta_{\ell_2} - \beta_\ell = O(h^3)$ when $\ell < \ell_2$, hence

$$\tau_{\ell_2} = O(h^{3(\ell_2 - 1)}), \quad \ell_2 = 2, 3, 4, 5,$$

in smooth regions. This fact is important for the WENO approximation in maintaining accuracy.

For our one-dimensional finite difference scheme (2.3), the numerical flux $\hat{f}^+_{i+1/2}$ in (2.4) is obtained by using the *Reconstruction Algorithm* with $\bar{w}_j = f^+(u_j)$ to obtain $w_i(x)$, and then by setting $\hat{f}^+_{i+1/2} = w_i(x_{i+1/2})$. The reconstruction of the numerical flux $\hat{f}^-_{i+1/2}$ is mirror-symmetric with respect to $x_{i+1/2}$. Finally, the semidiscrete scheme (2.3) is discretized by a third-order TVD Runge–Kutta time discretization method [46]

$$\begin{cases} u^{(1)} = u^n + \Delta t L(u^n), \\ u^{(2)} = \frac{3}{4}u^n + \frac{1}{4}u^{(1)} + \frac{1}{4}\Delta t L(u^{(1)}), \\ u^{n+1} = \frac{1}{3}u^n + \frac{2}{3}u^{(2)} + \frac{2}{3}\Delta t L(u^{(2)}), \end{cases} \tag{2.24}$$

to obtain a fully discrete scheme.

Next, we use the two-dimensional hyperbolic conservation laws

$$\begin{cases} u_t + f(u)_x + g(u)_y = 0, \\ u(x, y, 0) = u_0(x, y), \end{cases} \tag{2.25}$$

as an example to explain the new high-order finite difference WENO schemes. Thus we approximate the first equation of (2.25) as (2.2), where $L(u)$ is a high-order spatial discretization of $-f(u)_x - g(u)_y$. For simplicity, we use a uniform mesh (x_i, y_k) with $h = x_{i+1} - x_i = y_{k+1} - y_k$ as the mesh size. We also denote the half points as $x_{i+1/2} = \frac{1}{2}(x_i + x_{i+1})$, $y_{k+1/2} = \frac{1}{2}(y_k + y_{k+1})$. $u_{i,k}(t)$ is the numerical approximation to the nodal point value $u(x_i, y_k, t)$ of the exact solution. For conservation, the right hand side of (2.2) is written as

$$\frac{du_{i,k}(t)}{dt} = L(u)_{i,k} = -\frac{1}{h}(\hat{f}_{i+1/2,k} - \hat{f}_{i-1/2,k}) - \frac{1}{h}(\hat{g}_{i,k+1/2} - \hat{g}_{i,k-1/2}), \tag{2.26}$$

where $\hat{f}_{i+1/2,k}$ and $\hat{g}_{i,k+1/2}$ are the numerical fluxes. We use the third-order, fifth-order, seventh-order, and ninth-order versions as examples in this paper, thus we require $\frac{1}{h}(\hat{f}_{i+1/2,k} - \hat{f}_{i-1/2,k})$ to be an associated order approximation to $f(u)_x$ and $\frac{1}{h}(\hat{g}_{i,k+1/2} - \hat{g}_{i,k-1/2})$ to be the same order approximation to $g(u)_y$ at (x_i, y_k), respectively. For upwinding and stability, we often split the flux $f(u)$ into $f(u) = f^+(u) + f^-(u)$ with $\frac{df^+(u)}{du} \geq 0$ and $\frac{df^-(u)}{du} \leq 0$, and then approximate each of them separately using its own wind direction in the x-direction. The simple Lax–Friedrichs flux splitting $f^{\pm}(u) = \frac{1}{2}(f(u) \pm \alpha u)$ is used again in this paper, in which α is set as $\max_u |f'(u)|$ over the whole range of u in the x-direction. Likewise for $g(u)$ in the y-direction. Thus the numerical fluxes are also split accordingly

$$\hat{f}_{i+1/2,k} = \hat{f}^+_{i+1/2,k} + \hat{f}^-_{i+1/2,k}, \quad \hat{g}_{i,k+1/2} = \hat{g}^+_{i,k+1/2} + \hat{g}^-_{i,k+1/2}. \tag{2.27}$$

For our two-dimensional finite difference scheme (2.26), the numerical flux $\hat{f}^+_{i+1/2,k}$ in (2.27) is obtained by using the *Reconstruction Algorithm* with $\bar{w}_j = f^+(u_{j,k})$ to obtain $w_i(x)$, and then by setting $\hat{f}^+_{i+1/2,k} = w_i(x_{i+1/2})$. The construction of the numerical flux $\hat{f}^-_{i+1/2,k}$ is mirror-symmetric with respect to $x_{i+1/2}$, and the procedure for $g(u)_y$ in the y-direction is similar. Finally, the semidiscrete scheme (2.26) is discretized in time by (2.24).

For more details of the finite difference WENO schemes, we refer to [25,44,45]. Such new type of finite difference WENO schemes keeps the shock transition sharply in nonsmooth regions. We only use a series of unequal-sized central spatial stencils hierarchically without introducing any biased spatial stencils to control spurious oscillations. For the simulations of Euler equations, all of the reconstruction procedures are performed in the local characteristic directions to avoid spurious oscillations near discontinuities. We do not give further details and again refer the readers to [25,44,45].

2.2. Finite volume multi-resolution WENO schemes

We design the finite volume method for one-dimensional hyperbolic conservation laws (2.1). The computational mesh is distributed as before. We define the one-dimensional cell averages as $\bar{u}_i(t) = \frac{1}{h}\int_{x_i-h/2}^{x_i+h/2} u(\xi, t)d\xi$ and use $\bar{w}$ to denote the cell averaging operator. We integrate (2.1) over the target cell $I_i = [x_{i-1/2}, x_{i+1/2}]$ and obtain the integral formulation

$$\frac{d\bar{u}_i(t)}{dt} = -\frac{1}{h}\left(f(u(x_{i+1/2}, t)) - f(u(x_{i-1/2}, t))\right). \tag{2.28}$$

We approximate (2.28) by the following semi-discrete conservative scheme

$$\frac{d\bar{u}_i(t)}{dt} = L(u)_i = -\frac{1}{h}(\hat{f}_{i+1/2} - \hat{f}_{i-1/2}), \tag{2.29}$$

where the numerical flux $\hat{f}_{i+1/2}$ is defined by

$$\hat{f}_{i+1/2} = \hat{f}(u^-_{i+1/2}, u^+_{i+1/2}), \tag{2.30}$$

with the values $u^{\pm}_{i+1/2}$ obtained by the WENO reconstruction procedure. We also apply the Lax–Friedrichs flux

$$\hat{f}(a, b) = \frac{1}{2}[f(a) + f(b) - \alpha(b - a)], \tag{2.31}$$

where $\alpha = max_u|f'(u)|$ is a constant and the maximum is taken over the whole range of u.

For our one-dimensional finite volume scheme (2.29), the reconstruction procedure to obtain $u^-_{i+\frac{1}{2}}$ to approximate $u(x_{i+1/2}, t)$ from the third-order to ninth-order is obtained by using the *Reconstruction Algorithm* with $\bar{w}_j = \bar{u}_j$ for all j. After these point values are obtained, we can use the scheme (2.29) with the flux defined by (2.30), together with the Runge–Kutta time discretization (2.24), to advance in time.

Hereafter, we design the finite volume method for two-dimensional hyperbolic conservation laws (2.25). For simplicity, the grid meshes are uniformly divided into cells, and the cell sizes are $h = x_{i+\frac{1}{2}} - x_{i-\frac{1}{2}} = y_{k+\frac{1}{2}} - y_{k-\frac{1}{2}}$, with the cell centers $(x_i, y_k) = (\frac{1}{2}(x_{i-\frac{1}{2}} + x_{i+\frac{1}{2}}), \frac{1}{2}(y_{k-\frac{1}{2}} + y_{k+\frac{1}{2}}))$. We denote the two-dimensional cells by $I_{i,k} = I_i \times J_k = [x_{i-\frac{1}{2}}, x_{i+\frac{1}{2}}] \times [y_{k-\frac{1}{2}}, y_{k+\frac{1}{2}}]$ and define the two-dimensional cell averages as $\tilde{\bar{u}}_{i,k}(t) = \frac{1}{h^2}\int_{y_k-h/2}^{y_k+h/2}\int_{x_i-h/2}^{x_i+h/2} u(x, y, t)dxdy$, where we use $\bar{w}$ to denote the cell averaging operator in the x-direction and $\tilde{w}$ to denote the cell averaging operator in the y-direction. We integrate (2.25) over target cell $I_{i,k}$ and obtain the integral formulation

$$\frac{d\tilde{\bar{u}}_{i,k}(t)}{dt} = -\frac{1}{h^2}\left(\int_{y_k-h/2}^{y_k+h/2} f(u(x_{i+1/2}, y, t))dy - \int_{y_k-h/2}^{y_k+h/2} f(u(x_{i-1/2}, y, t))dy + \int_{x_i-h/2}^{x_i+h/2} g(u(x, y_{k+1/2}, t))dx - \int_{x_i-h/2}^{x_i+h/2} g(u(x, y_{k-1/2}, t))dx\right). \tag{2.32}$$

We approximate (2.32) by the following semi-discrete conservative scheme

$$\frac{d\tilde{\bar{u}}_{i,k}(t)}{dt} = L(u)_{i,k} = -\frac{1}{h}(\hat{f}_{i+1/2,k} - \hat{f}_{i-1/2,k}) - \frac{1}{h}(\hat{g}_{i,k+1/2} - \hat{g}_{i,k-1/2}), \tag{2.33}$$

where the numerical fluxes $\hat{f}_{i+1/2,k}$ and $\hat{g}_{i,k+1/2}$ are defined as

$$\begin{aligned}\hat{f}_{i+1/2,k} &= \textstyle\sum_{\ell=1}^{\kappa} \varpi_\ell \hat{f}(u^-_{i+1/2,k+\sigma_\ell}, u^+_{i+1/2,k+\sigma_\ell}),\\ \hat{g}_{i,k+1/2} &= \textstyle\sum_{\ell=1}^{\kappa} \varpi_\ell \hat{g}(u^-_{i+\sigma_\ell,k+1/2}, u^+_{i+\sigma_\ell,k+1/2}),\end{aligned} \tag{2.34}$$

to approximate $\frac{1}{h}\int_{y_k-h/2}^{y_k+h/2} f(u(x_{i+1/2}, y, t))dy$ and $\frac{1}{h}\int_{x_i-h/2}^{x_i+h/2} g(u(x, y_{k+1/2}, t))dx$, respectively. ϖ_ℓ and σ_ℓ are κ-point Gaussian quadrature weights and nodes in the cell $[-\frac{1}{2}, \frac{1}{2}]$ ($\kappa = 2$, $\kappa = 3$, $\kappa = 4$, and $\kappa = 5$ for the third-order, fifth-order, seventh-order, and ninth-order approximations, respectively). The numerical fluxes $\hat{f}(a, b)$ and $\hat{g}(a, b)$ are defined as the simple Lax–Friedrichs flux (2.31). $u^{\pm}_{i+1/2,k+\sigma_\ell}$ and $u^{\pm}_{i+\sigma_\ell,k+1/2}$ are the associated order approximations of $u(x^{\pm}_{i+1/2}, y_{k+\sigma_\ell}, t)$ and $u(x_{i+\sigma_\ell}, y^{\pm}_{k+1/2}, t)$, respectively, which will be reconstructed by the WENO procedure.

Unfortunately, even though the building block of finite volume WENO schemes is still the simple *Reconstruction Algorithm* as given in the previous section, this algorithm must be used multiple times in order to "de-cell average" from the two-dimensional cell averages $\tilde{\bar{u}}_{i,k}$ to the point values $u^{\pm}_{i+1/2,k+\sigma_\ell}$ etc. at the Gaussian quadrature points along cell boundaries. For example, to obtain $u^-_{i+1/2,k+\sigma_\ell}$ and $u^+_{i-1/2,k+\sigma_\ell}$, the following procedure is followed:

(1) For each k, take $\bar{w}_j = \tilde{\bar{u}}_{j,k}$ and use the *Reconstruction Algorithm* to obtain $w_i(x)$, then identify $\tilde{u}^-_{i+1/2,k} = w_i(x_{i+1/2})$ and $\tilde{u}^+_{i-1/2,k} = w_i(x_{i-1/2})$, respectively, which are the y-cell averages of u at $x = x^-_{i+1/2}$ and at $x = x^+_{i-1/2}$, respectively;

(2) For each $i + 1/2$, take $\tilde{w}_j = \tilde{u}^-_{i+1/2,j}$ and use the *Reconstruction Algorithm* to obtain the polynomial $w_k(y)$, then identify $u^-_{i+1/2,k+\sigma_\ell} = w_k(y_k + \sigma_\ell h)$ at all Gaussian points. Similarly, take $\tilde{w}_j = \tilde{u}^+_{i-1/2,j}$ and use the *Reconstruction Algorithm* to obtain the polynomial $w_k(y)$, then identify $u^+_{i-1/2,k+\sigma_\ell} = w_k(y_k + \sigma_\ell h)$ at all Gaussian points.

After these point values at the Gaussian points are obtained, we can use the scheme (2.33) with the fluxes defined by (2.34), together with the Runge–Kutta time discretization (2.24), to advance in time. In the reconstruction above, local characteristic decomposition is used to avoid spurious oscillations. We again refer to [43–45] for more details. We can easily extend such high-order finite volume WENO schemes to arbitrary higher order accuracy and to higher dimensions in a dimension-by-dimension manner. Since the same linear weights are set at all Gaussian quadrature points on the boundaries of the target cell $I_{i,k}$, we can reduce the cost of the spatial reconstruction procedure in comparison to the classical finite volume WENO schemes, for which the linear weights are different for different quadrature points.

3. Numerical tests

In this section, we present the results of numerical tests of the new fifth-order, seventh-order, and ninth-order finite difference and finite volume multi-resolution WENO schemes which are termed as WENOκ-FD and WENOκ-FV schemes

Table 3.1
$\mu_t + (\frac{\mu^2}{2})_x = 0$. Initial data $\mu(x,0) = 0.5 + \sin(\pi x)$. WENO-FD and WENO-FV schemes. $T = 0.5/\pi$. L^1 and L^∞ errors.

	WENO5-FD scheme				WENO7-FD scheme			
Grid points	L^1 error	Order	L^∞ error	Order	L^1 error	Order	L^∞ error	Order
100	8.96E−7		1.02E−5		6.08E−8		9.42E−7	
120	3.33E−7	5.42	4.02E−6	5.11	1.70E−8	6.97	2.95E−7	6.36
140	1.49E−7	5.20	1.86E−6	4.98	5.91E−9	6.89	9.90E−8	7.09
160	7.40E−8	5.28	9.32E−7	5.20	2.28E−9	7.11	3.98E−8	6.82
180	3.98E−8	5.24	5.18E−7	4.98	1.00E−9	7.02	1.73E−8	7.04
200	2.31E−8	5.18	3.03E−7	5.09	4.71E−10	7.15	8.29E−9	7.01

	WENO9-FD scheme			
Grid points	L^1 error	Order	L^∞ error	Order
100	9.36E−9		1.80E−7	
120	1.97E−9	8.54	3.69E−8	8.69
140	5.15E−10	8.71	1.03E−8	8.24
160	1.58E−10	8.84	3.07E−9	9.11
180	5.47E−11	9.02	1.12E−9	8.57
200	2.11E−11	9.02	4.35E−10	8.97

	WENO5-FV scheme				WENO7-FV scheme			
Grid cells	L^1 error	Order	L^∞ error	Order	L^1 error	Order	L^∞ error	Order
100	6.73E−7		7.50E−6		4.29E−8		7.00E−7	
120	2.65E−7	5.11	3.24E−6	4.59	1.28E−8	6.60	2.08E−7	6.64
140	1.21E−7	5.09	1.52E−6	4.89	4.50E−9	6.82	7.59E−8	6.55
160	6.17E−8	5.04	7.93E−7	4.90	1.80E−9	6.86	3.02E−8	6.89
180	3.44E−8	4.96	4.41E−7	4.97	8.10E−10	6.78	1.38E−8	6.64
200	2.02E−8	5.02	2.62E−7	4.95	3.95E−10	6.82	6.67E−9	6.92

	WENO9-FV scheme			
Grid cells	L^1 error	Order	L^∞ error	Order
100	5.85E−9		1.10E−7	
120	1.31E−9	8.17	2.34E−8	8.51
140	3.62E−10	8.39	7.12E−9	7.73
160	1.15E−10	8.56	2.18E−9	8.85
180	4.15E−11	8.67	8.28E−10	8.23
200	1.64E−11	8.78	3.31E−10	8.69

($\kappa = 5, 7, 9$), respectively, as specified in the previous section. The numerical results of the third-order WENO schemes are omitted for simplicity. The CFL number is set as 0.6 for all examples, except for the accuracy tests where the time step is smaller so as to guarantee that the spatial error dominates. As mentioned before, we take the linear weights as $\bar{\gamma}_{1,3} = 1$, $\bar{\gamma}_{2,3} = 10$, and $\bar{\gamma}_{3,3} = 100$ for WENO5 schemes; $\bar{\gamma}_{1,4} = 1$, $\bar{\gamma}_{2,4} = 10$, $\bar{\gamma}_{3,4} = 100$, and $\bar{\gamma}_{4,4} = 1000$ for WENO7 schemes; $\bar{\gamma}_{1,5} = 1$, $\bar{\gamma}_{2,5} = 10$, $\bar{\gamma}_{3,5} = 100$, $\bar{\gamma}_{4,5} = 1000$, and $\bar{\gamma}_{5,5} = 10000$ for WENO9 schemes, respectively.

Example 3.1. We solve the following nonlinear scalar Burgers' equation

$$\mu_t + (\frac{\mu^2}{2})_x = 0, \quad 0 < x < 2, \tag{3.1}$$

with the initial condition $\mu(x,0) = 0.5 + \sin(\pi x)$ and periodic boundary condition. When $t = 0.5/\pi$ the solution is still smooth, and the errors and numerical orders of accuracy by different WENO schemes are shown in Table 3.1. We can see that all of the finite difference and finite volume WENO schemes achieve their designed order of accuracy. The errors from the finite volume schemes are smaller than those from the finite difference schemes on the same meshes. This might be due to a smaller numerical viscosity in the finite volume WENO reconstruction procedure than that in the finite difference framework, as these two procedures act on different functions (the finite volume procedure acts on cell averages of the solutions and the finite difference procedure acts on point values of the nonlinear fluxes).

Example 3.2. Next, we solve the following two-dimensional nonlinear scalar Burgers' equation

$$\mu_t + (\frac{\mu^2}{2})_x + (\frac{\mu^2}{2})_y = 0, \quad 0 < x, y < 4, \tag{3.2}$$

with the initial condition $\mu(x,y,0) = 0.5 + \sin(\pi(x+y)/2)$ and periodic boundary conditions. When $t = 0.5/\pi$ the solution is still smooth, and the errors and numerical orders of accuracy by different WENO schemes are shown in Table 3.2. We can see that, once again, these finite difference and finite volume WENO schemes achieve their designed order of accuracy.

Table 3.2
$\mu_t + (\frac{\mu^2}{2})_x + (\frac{\mu^2}{2})_y = 0$. Initial data $\mu(x, y, 0) = 0.5 + \sin(\pi(x + y)/2)$. WENO-FD and WENO-FV schemes. $T = 0.5/\pi$. L^1 and L^∞ errors.

	WENO5-FD scheme				WENO7-FD scheme			
Grid points	L^1 error	Order	L^∞ error	Order	L^1 error	Order	L^∞ error	Order
100 × 100	1.19E−6		1.02E−5		6.14E−8		9.42E−7	
120 × 120	3.35E−7	6.95	4.02E−6	5.10	1.72E−8	6.98	2.95E−7	6.36
140 × 140	1.53E−7	5.05	1.86E−6	4.99	5.95E−9	6.89	9.90E−8	7.09
160 × 160	7.34E−8	5.54	9.31E−7	5.20	2.30E−9	7.11	3.98E−8	6.82
180 × 180	4.02E−8	5.11	5.18E−7	4.98	1.00E−9	7.02	1.73E−8	7.04
200 × 200	2.32E−8	5.22	3.03E−7	5.08	4.73E−10	7.16	8.29E−9	7.01

	WENO9-FD scheme			
Grid points	L^1 error	Order	L^∞ error	Order
100 × 100	1.00E−8		1.90E−7	
120 × 120	2.12E−9	8.51	3.94E−8	8.65
140 × 140	5.56E−10	8.70	1.10E−8	8.23
160 × 160	1.70E−10	8.84	3.29E−9	9.08
180 × 180	5.89E−11	9.03	1.20E−9	8.55
200 × 200	2.27E−11	9.04	4.67E−10	8.97

	WENO5-FV scheme				WENO7-FV scheme			
Grid cells	L^1 error	Order	L^∞ error	Order	L^1 error	Order	L^∞ error	Order
100 × 100	6.81E−7		7.53E−6		4.10E−8		6.28E−7	
120 × 120	2.55E−7	5.37	3.09E−6	4.87	1.22E−8	6.62	2.03E−7	6.17
140 × 140	1.19E−7	4.93	1.49E−6	4.72	4.42E−9	6.61	7.27E−8	6.68
160 × 160	6.10E−8	5.04	7.70E−7	4.97	1.78E−9	6.80	3.00E−8	6.62
180 × 180	3.41E−8	4.94	4.36E−7	4.83	7.97E−10	6.84	1.35E−8	6.76
200 × 200	2.00E−8	5.04	2.60E−7	4.90	3.84E−10	6.93	6.62E−9	6.80

	WENO9-FV scheme			
Grid cells	L^1 error	Order	L^∞ error	Order
100 × 100	6.02E−9		1.11E−7	
120 × 120	1.39E−9	8.04	2.45E−8	8.32
140 × 140	3.84E−10	8.34	7.47E−9	7.70
160 × 160	1.22E−10	8.54	2.30E−9	8.83
180 × 180	4.44E−11	8.64	8.85E−10	8.11
200 × 200	1.76E−11	8.77	3.54E−10	8.69

Example 3.3. We consider the following one-dimensional Euler equations

$$\frac{\partial}{\partial t}\begin{pmatrix}\rho\\ \rho\mu\\ E\end{pmatrix} + \frac{\partial}{\partial x}\begin{pmatrix}\rho\mu\\ \rho\mu^2 + p\\ \mu(E+p)\end{pmatrix} = 0 \tag{3.3}$$

in which ρ is the density, μ is the velocity, E is the total energy, and p is the pressure. The initial conditions are $\rho(x, 0) = 1 + 0.2\sin(x)$, $\mu(x, 0) = 1$, $p(x, 0) = 1$, and $\gamma = 1.4$. The computational domain is $[0, 2\pi]$. Periodic boundary condition is applied. The exact solution is $\rho(x, t) = 1 + 0.2\sin(x - t)$. The final time is $t = 2$. The errors and numerical orders of accuracy of the density by the new WENO schemes are shown in Table 3.3. We can observe that the theoretical order of accuracy is achieved.

Example 3.4. Next, we consider the following two-dimensional Euler equations

$$\frac{\partial}{\partial t}\begin{pmatrix}\rho\\ \rho\mu\\ \rho\nu\\ E\end{pmatrix} + \frac{\partial}{\partial x}\begin{pmatrix}\rho\mu\\ \rho\mu^2 + p\\ \rho\mu\nu\\ \mu(E+p)\end{pmatrix} + \frac{\partial}{\partial y}\begin{pmatrix}\rho\nu\\ \rho\mu\nu\\ \rho\nu^2 + p\\ \nu(E+p)\end{pmatrix} = 0 \tag{3.4}$$

in which ρ is the density; μ and ν are the velocities in the x- and y-directions, respectively; E is the total energy; and p is the pressure. The initial conditions are: $\rho(x, y, 0) = 1 + 0.2\sin(x + y)$, $\mu(x, y, 0) = 1$, $\nu(x, y, 0) = 1$, $p(x, y, 0) = 1$. The computational domain is $[0, 2\pi] \times [0, 2\pi]$. Periodic boundary conditions are applied in both directions. The exact solution is $\rho(x, y, t) = 1 + 0.2\sin(x + y - 2t)$. We compute the solution up to $t = 2$. The errors and numerical orders of accuracy of the density by different finite difference and finite volume WENO schemes are shown in Table 3.4. We can observe that the theoretical order of accuracy is achieved in this two-dimensional test case.

Table 3.3
1D-Euler equations: initial data $\rho(x,0)=1+0.2\sin(x)$, $\mu(x,0)=1$ and $p(x,0)=1$. WENO-FD and WENO-FV schemes. $T=2$. L^1 and L^∞ errors.

	WENO5-FD scheme				WENO7-FD scheme			
Grid points	L^1 error	Order	L^∞ error	Order	L^1 error	Order	L^∞ error	Order
10	4.17E−3		7.80E−3		3.05E−4		7.80E−4	
20	4.00E−4	3.38	1.28E−3	2.60	7.50E−7	8.67	1.19E−6	9.35
30	4.32E−5	5.48	1.50E−4	5.29	4.42E−8	6.98	7.20E−8	6.93
40	2.53E−6	9.86	1.74E−5	7.49	5.92E−9	6.99	9.47E−9	7.05
50	6.81E−7	5.88	3.78E−6	6.83	1.24E−9	6.99	1.95E−9	7.07
60	2.03E−7	6.62	1.41E−6	5.40	3.47E−10	6.99	5.44E−10	7.01

	WENO9-FD scheme			
Grid points	L^1 error	Order	L^∞ error	Order
10	1.19E−5		2.92E−5	
20	1.93E−8	9.27	2.93E−8	9.96
30	5.06E−10	8.98	7.83E−10	8.94
40	3.80E−11	9.00	5.92E−11	8.98
50	5.11E−12	9.00	7.95E−12	9.00
60	9.91E−13	8.99	1.56E−12	8.93

	WENO5-FV scheme				WENO7-FV scheme			
Grid cells	L^1 error	Order	L^∞ error	Order	L^1 error	Order	L^∞ error	Order
10	1.73E−3		4.70E−3		8.40E−5		1.35E−4	
20	1.29E−4	3.75	3.88E−4	3.60	7.26E−7	6.85	1.19E−6	6.83
30	1.62E−5	5.11	5.29E−5	4.92	4.36E−8	6.93	6.87E−8	7.04
40	1.36E−6	8.62	6.40E−6	7.34	5.87E−9	6.97	9.21E−9	6.98
50	3.44E−7	6.16	1.53E−6	6.40	1.23E−9	6.99	1.93E−9	6.98
60	1.38E−7	5.00	4.50E−7	6.72	3.44E−10	6.99	5.41E−10	6.99

	WENO9-FV scheme			
Grid cells	L^1 error	Order	L^∞ error	Order
10	7.62E−6		1.26E−5	
20	1.51E−8	8.97	2.39E−8	9.05
30	3.98E−10	8.97	6.25E−10	8.99
40	3.00E−11	8.99	4.70E−11	8.99
50	4.02E−12	9.00	6.33E−12	8.99
60	7.81E−13	8.99	1.25E−12	8.89

Example 3.5. We solve one-dimensional Euler equations (3.3) with Riemann initial condition for the Lax problem

$$(\rho,\mu,p,\gamma)^T=\begin{cases}(0.445,0.698,3.528,1.4)^T, & x\in[-0.5,0),\\ (0.5,0,0.571,1.4)^T, & x\in[0,0.5].\end{cases} \tag{3.5}$$

For $t=0.16$, we present the computed density ρ obtained with different finite difference and finite volume WENO schemes in Fig. 3.1 and Fig. 3.2. We observe that all the new WENO schemes work well in comparison with the exact solution.

Example 3.6. The shock density wave interaction problem [45]. We solve one-dimensional Euler equations (3.3) with a moving Mach = 3 shock interacting with sine waves in density: $(\rho,\mu,p,\gamma)^T=(3.857143,2.629369,10.333333,1.4)^T$ for $x\in[-5,-4)$; $(\rho,\mu,p,\gamma)^T=(1+0.2\sin(5x),0,1,1.4)^T$ for $x\in[-4,5]$. The referenced "exact" solution which is a converged solution computed by the finite difference fifth order WENO scheme [25] with 2000 grid points is plotted in Fig. 3.3 and Fig. 4.1. The results for the fifth-order, seventh-order, and ninth-order finite difference and finite volume WENO schemes are also shown in Fig. 3.3 and Fig. 4.1, respectively. These WENO schemes could get good resolution in comparison with the reference "exact" solution. Again, it appears that the finite volume WENO schemes have better resolution than the finite difference WENO schemes on the same mesh for this example.

Example 3.7. We now consider the interaction of two blast waves. The initial conditions are

$$(\rho,\mu,p,\gamma)^T=\begin{cases}(1,0,10^3,1.4)^T, & 0<x<0.1,\\ (1,0,10^{-2},1.4)^T, & 0.1<x<0.9,\\ (1,0,10^2,1.4)^T, & 0.9<x<1.\end{cases} \tag{3.6}$$

The computed density ρ of different WENO schemes is plotted at $t=0.038$ against the reference "exact" solution which is a converged solution computed by the finite difference fifth order WENO scheme [25] with 20000 grid points in Fig. 4.2

Table 3.4
2D-Euler equations: initial data $\rho(x, y, 0) = 1 + 0.2\sin(x + y)$, $\mu(x, y, 0) = 1$, $\nu(x, y, 0) = 1$ and $p(x, y, 0) = 1$. WENO-FD and WENO-FV schemes. $T = 2$. L^1 and L^∞ errors.

	WENO5-FD scheme				WENO7-FD scheme			
Grid points	L^1 error	Order	L^∞ error	Order	L^1 error	Order	L^∞ error	order
10×10	4.74E−3		1.40E−2		3.11E−4		8.00E−4	
20×20	8.23E−4	2.52	2.43E−3	2.52	1.46E−6	7.73	2.49E−6	8.33
30×30	3.81E−5	7.58	1.28E−4	7.26	8.75E−8	6.95	1.50E−7	6.92
40×40	6.81E−6	5.98	3.29E−5	4.73	1.17E−8	6.98	1.87E−8	7.23
50×50	9.85E−7	8.66	5.04E−6	8.40	2.46E−9	7.00	3.89E−9	7.05
60×60	3.58E−7	5.55	2.00E−6	5.07	6.90E−10	6.98	1.08E−9	6.99

	WENO9-FD scheme			
Grid points	L^1 error	Order	L^∞ error	Order
10×10	3.08E−5		6.74E−5	
20×20	4.03E−8	9.57	6.37E−8	10.0
30×30	1.07E−9	8.95	1.67E−9	8.97
40×40	8.08E−11	8.98	1.26E−10	8.98
50×50	1.08E−11	8.99	1.70E−11	8.98
60×60	2.11E−12	8.98	3.33E−12	8.96

	WENO5-FV scheme				WENO7-FV scheme			
Grid cells	L^1 error	Order	L^∞ error	Order	L^1 error	Order	L^∞ error	order
10×10	3.82E−3		8.63E−3		3.20E−4		5.81E−4	
20×20	3.70E−4	3.37	1.50E−3	2.52	1.45E−6	7.78	2.34E−6	7.95
30×30	2.20E−5	6.96	1.19E−4	6.23	8.72E−8	6.94	1.37E−7	6.99
40×40	2.12E−6	8.12	9.02E−6	8.99	1.17E−8	6.97	1.83E−8	6.99
50×50	6.86E−7	5.07	2.26E−6	6.19	2.46E−9	6.99	3.86E−9	6.99
60×60	2.76E−7	4.98	8.09E−7	5.64	6.89E−10	6.98	1.08E−9	6.98

	WENO9-FV scheme			
Grid cells	L^1 error	Order	L^∞ error	Order
10×10	1.86E−5		2.89E−5	
20×20	4.00E−8	8.86	6.30E−8	8.84
30×30	1.06E−9	8.94	1.67E−9	8.95
40×40	8.07E−11	8.97	1.26E−10	8.98
50×50	1.08E−11	8.99	1.70E−11	8.98
60×60	2.10E−12	8.98	3.33E−12	8.94

and Fig. 4.3. These WENO schemes could give sharp shock transitions in comparison with the reference "exact" solution for this test case. Once again, it appears that the finite volume WENO schemes have better resolution than the finite difference WENO schemes on the same mesh for this example. We remark that the classical ninth-order WENO scheme on a uniform mesh of 800 grid points breaks down without using positivity-preserving limiters for this example.

Example 3.8. The Sedov blast wave problem. This problem contains very low density with strong shocks. The exact solution is specified in [27,39]. The computational domain is $[-2, 2]$ and initial conditions are $\rho = 1$, $\mu = 0$, $E = 10^{-12}$ everywhere except that the energy in the center cell is the constant $\frac{3200000}{\Delta x}$. The inlet and outlet conditions are imposed on the left and right boundaries, respectively. The final computational time is $t = 0.001$. The computational results by the finite difference and finite volume WENO schemes including the density, velocity, and pressure are shown in Fig. 4.4 and Fig. 4.5, respectively. We can see that these WENO schemes work well for this extreme test case without introducing any positivity preserving methods [2,50,53–56].

Example 3.9. Double Mach reflection problem [49]. We solve the Euler equations (3.4) in a computational domain of $[0, 4] \times [0, 1]$. A reflection wall lies at the bottom of the domain starting from $x = \frac{1}{6}$, $y = 0$, making a 60° angle with the x-axis. The reflection boundary condition is used at the wall, and for the rest of the bottom boundary (the part from $x = 0$ to $x = \frac{1}{6}$), the exact post-shock condition is imposed. The top boundary is the exact motion of the Mach 10 shock and $\gamma = 1.4$. The results are shown at $t = 0.2$. We only present the pictures of region $[0, 3] \times [0, 1]$ and the blow-up region around the double Mach stems in Fig. 4.6 and Fig. 4.7, and the zoomed-in pictures in Fig. 4.8. The WENO schemes could gain good density resolutions and sharp shock transitions with increasing order of accuracy from the fifth-order to ninth-order, respectively.

Example 3.10. A Mach 3 wind tunnel with a step problem [49]. The setup of the problem is as follows. The wind tunnel is one length unit wide and three length units long. The step is 0.2 length units high and is located 0.6 length units from

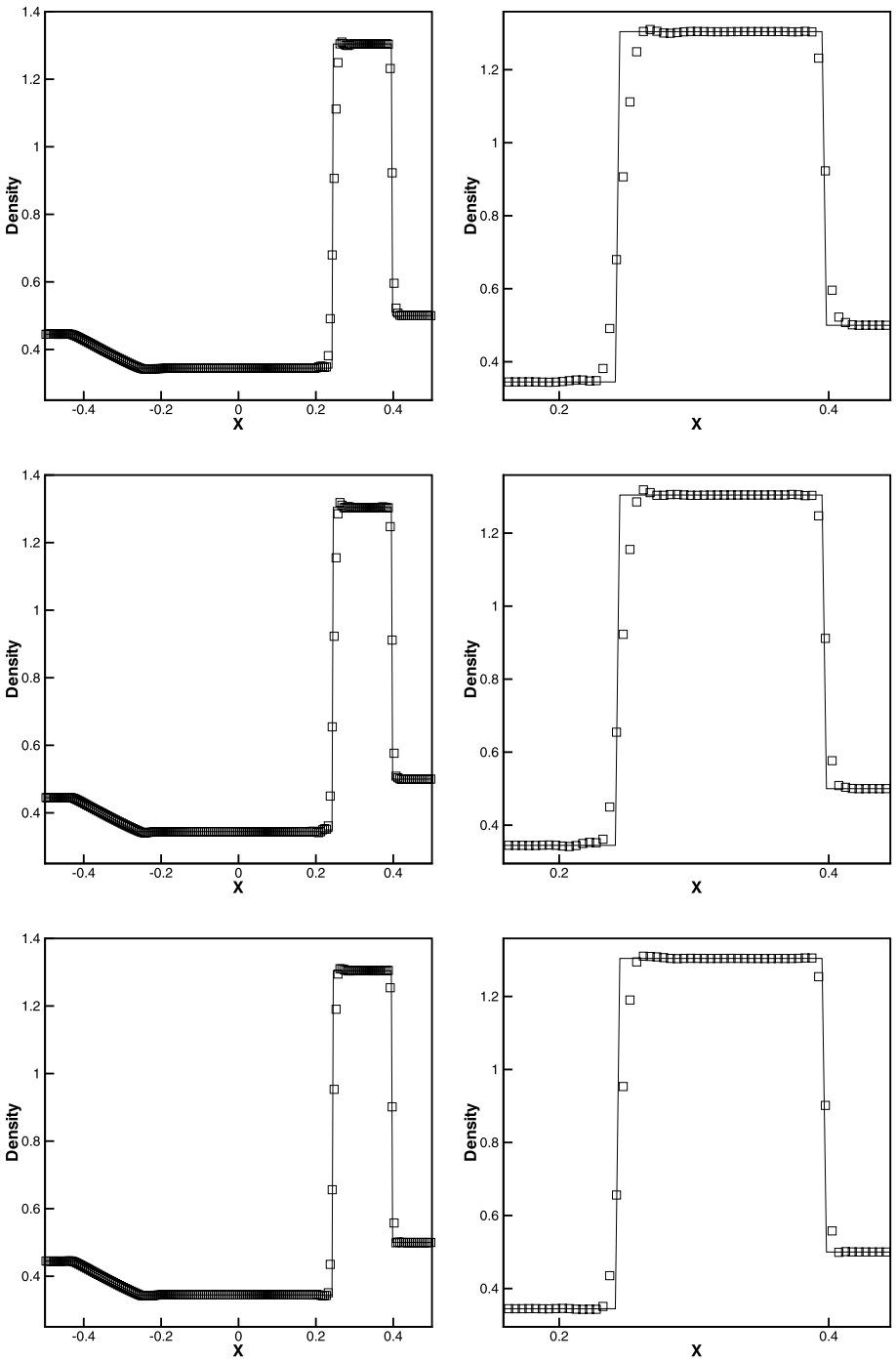

Fig. 3.1. The Lax problem. $T = 0.16$. From top to bottom: WENO5-FD, WENO7-FD, and WENO9-FD. Solid line: the exact solution; squares: the results of WENO schemes. Left: density; right: density zoomed in. Grid points: 200.

the left-hand end of the tunnel. The problem is initialized by a right-going Mach 3 flow. Reflective boundary conditions are applied along the wall of the tunnel and inflow/outflow boundary conditions are applied at the entrance/exit. The results are shown at $t = 4$. In Fig. 4.9 and Fig. 4.10, we show 30 equally spaced density contours from 0.32 to 6.15 computed by the new fifth-order, seventh-order, and ninth-order WENO schemes in the finite difference and finite volume frameworks. We can clearly find that all WENO schemes give good results especially for the high resolution of the physical instability and roll-up of the contact line.

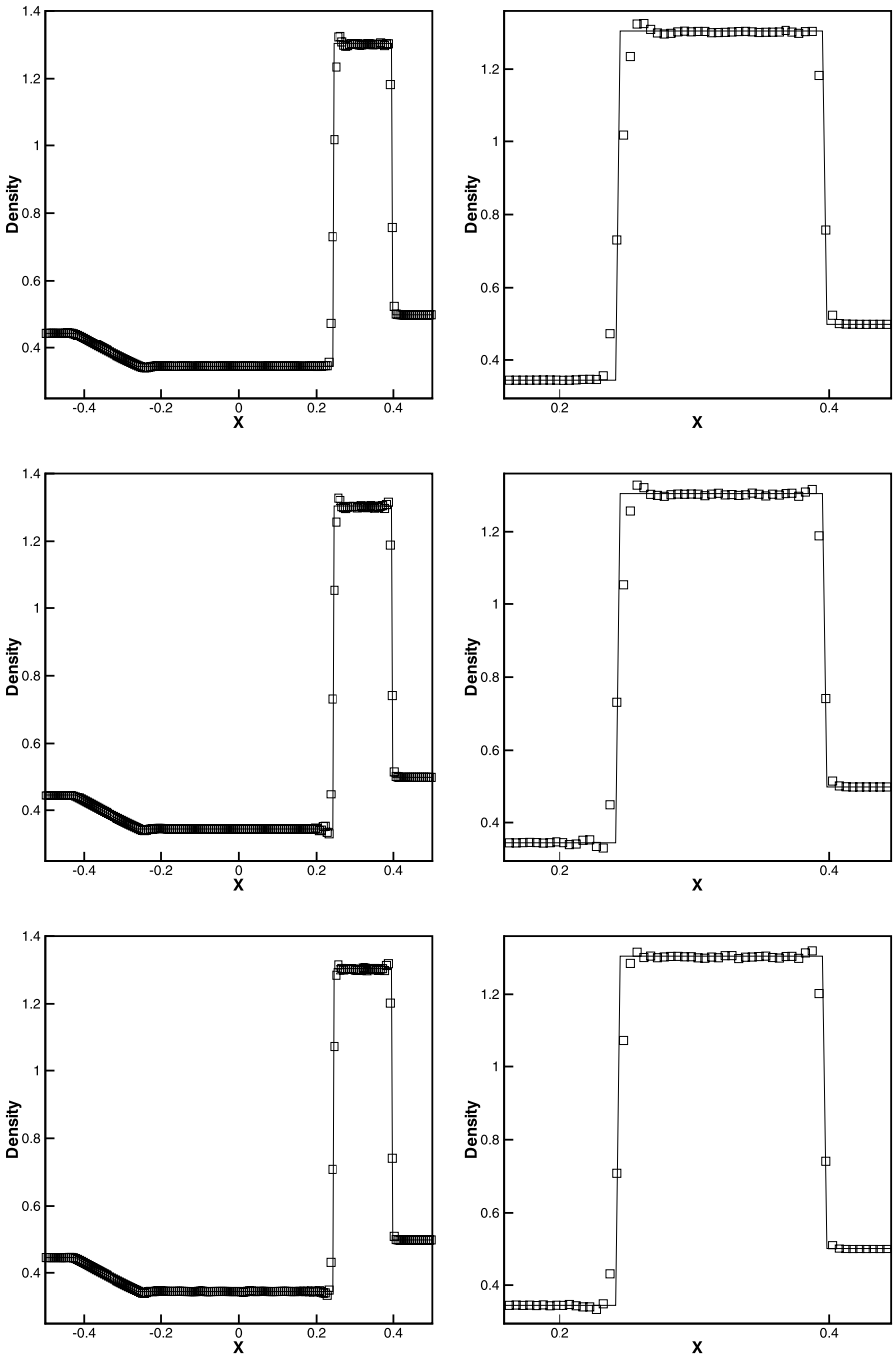

Fig. 3.2. The Lax problem. $T = 0.16$. From top to bottom: WENO5-FV, WENO7-FV, and WENO9-FV. Solid line: the exact solution; squares: the results of WENO schemes. Left: density; right: density zoomed in. Grid cells: 200.

4. Concluding remarks

In this paper, a new type of third-order, fifth-order, seventh-order, and ninth-order finite difference and finite volume multi-resolution WENO schemes is constructed for solving the hyperbolic conservation laws. The new features of these WENO schemes are their simplicity and hierarchical structure in obtaining increasingly higher order of accuracy with two, three, four, and five unequal sized hierarchical central spatial stencils. The WENO spatial reconstructions are adopted by artificially setting positive linear weights, calculating smoothness indicators, and designing new nonlinear weights as in [3,8]. The framework of this new class of multi-resolution WENO spatial reconstruction procedure would be particularly efficient and simple on unstructured meshes, the study of which is our ongoing work.

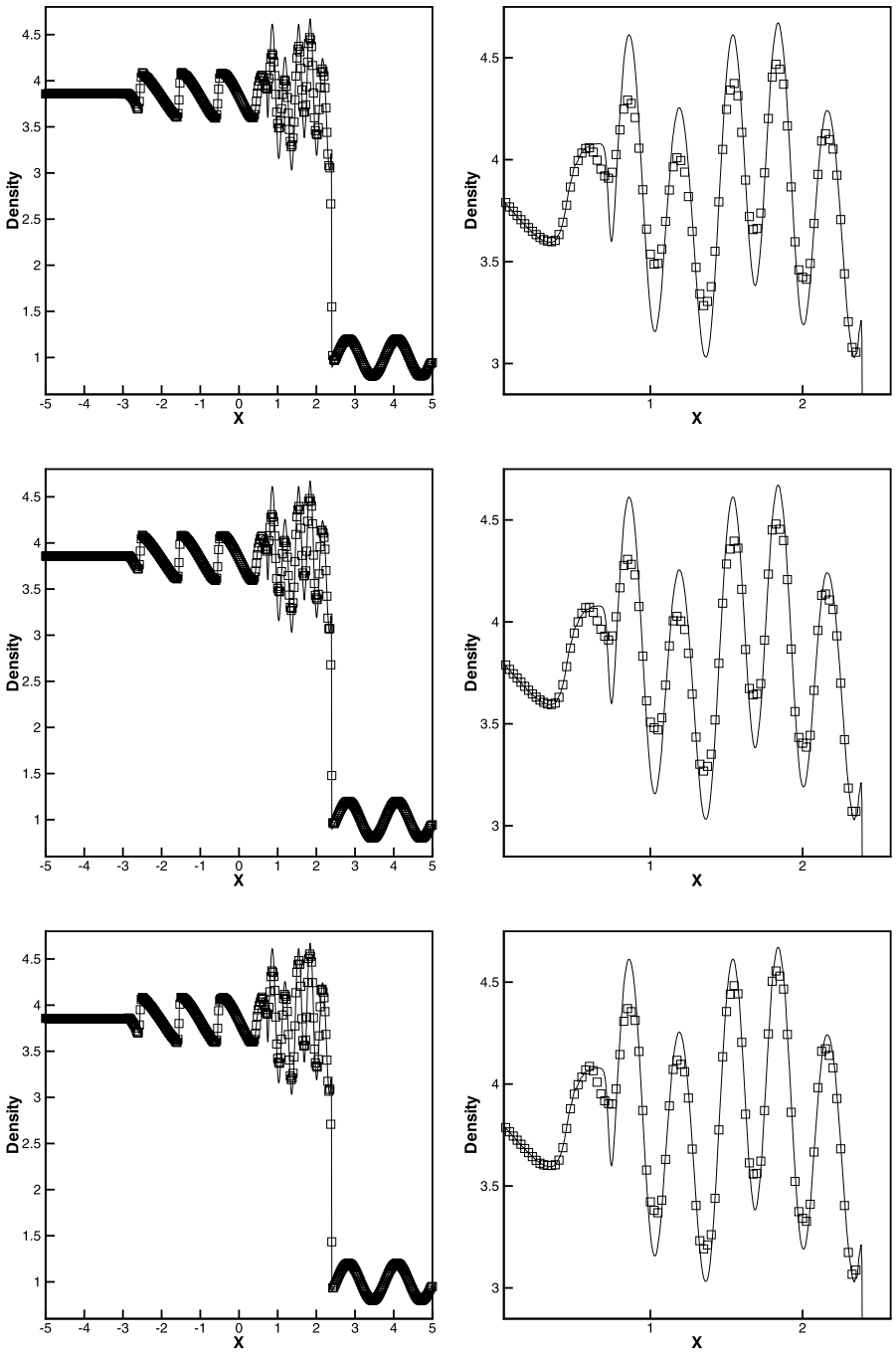

Fig. 3.3. The shock density wave interaction problem. $T = 1.8$. From top to bottom: WENO5-FD, WENO7-FD, and WENO9-FD. Solid line: the exact solution; squares: the results of WENO schemes. Left: density; right: density zoomed in. Grid points: 400.

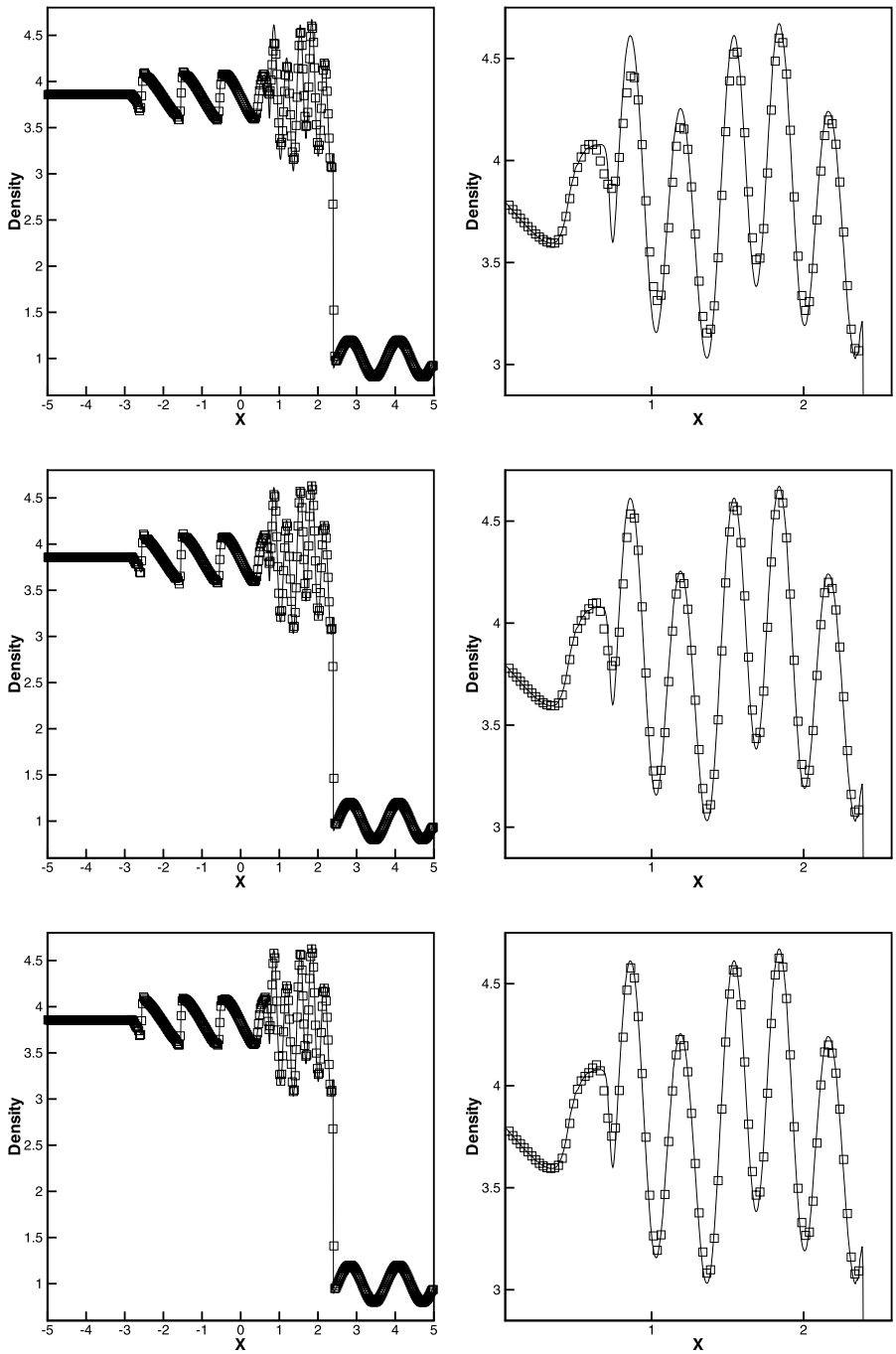

Fig. 4.1. The shock density wave interaction problem. $T = 1.8$. From top to bottom: WENO5-FV, WENO7-FV, and WENO9-FV. Solid line: the exact solution; squares: the results of WENO schemes. Left: density; right: density zoomed in. Grid cells: 400.

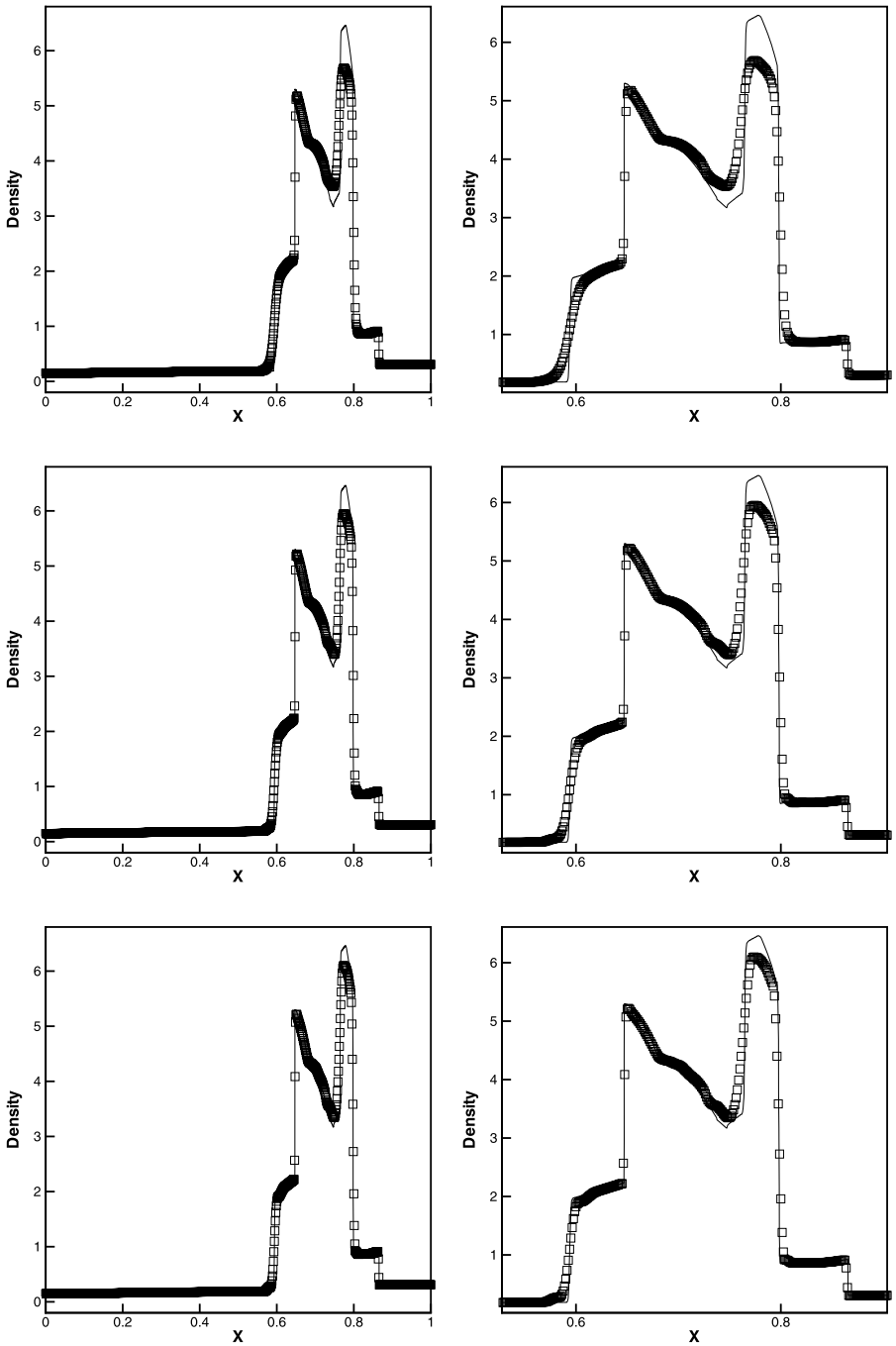

Fig. 4.2. The blast wave problem. $T = 0.038$. From top to bottom: WENO5-FD, WENO7-FD, and WENO9-FD. Solid line: the exact solution; squares: the results of WENO schemes. Left: density; right: density zoomed in. Grid points: 800.

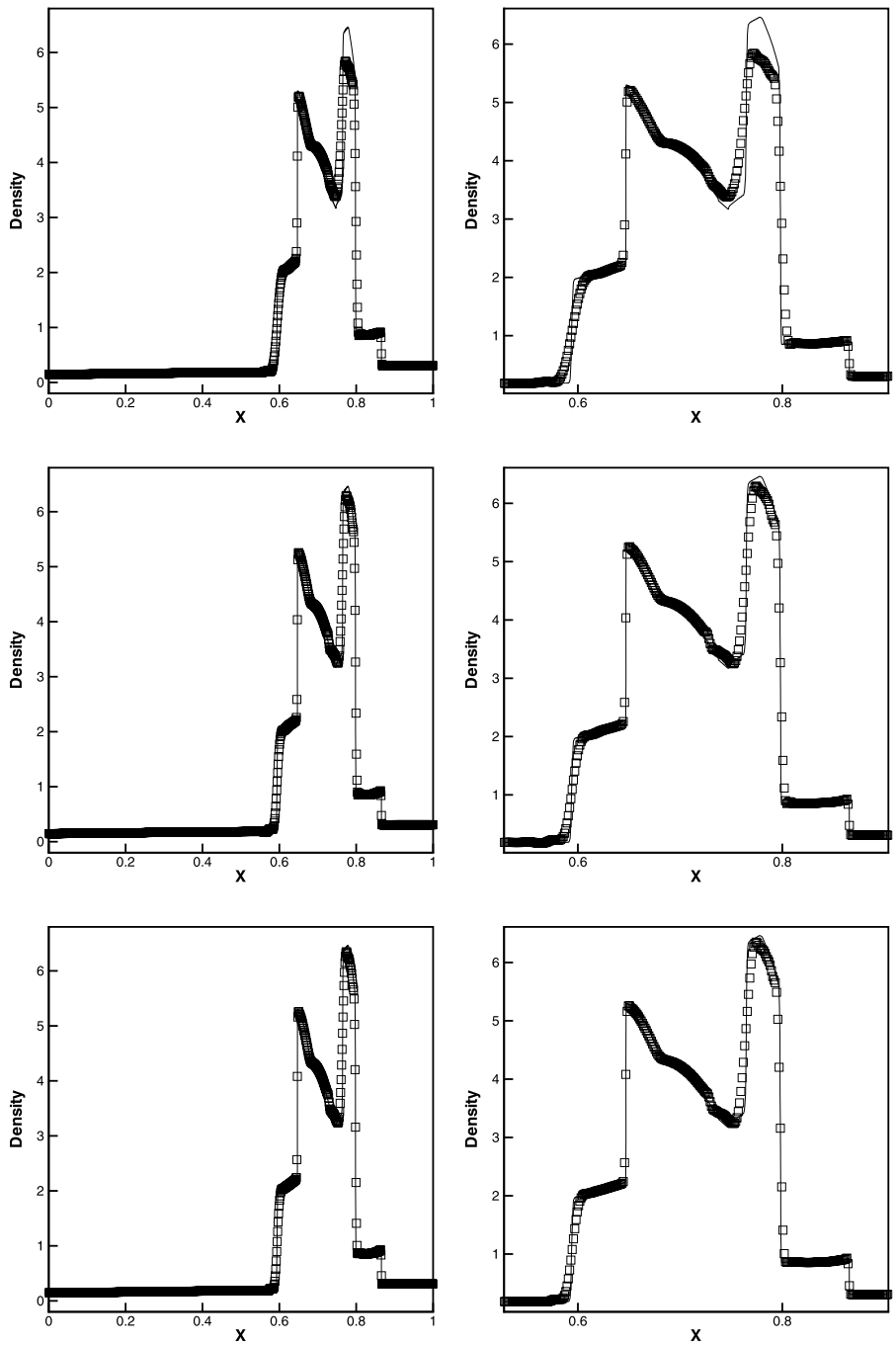

Fig. 4.3. The blast wave problem. $T = 0.038$. From top to bottom: WENO5-FV, WENO7-FV, and WENO9-FV. Solid line: the exact solution; squares: the results of WENO schemes. Left: density; right: density zoomed in. Grid cells: 800.

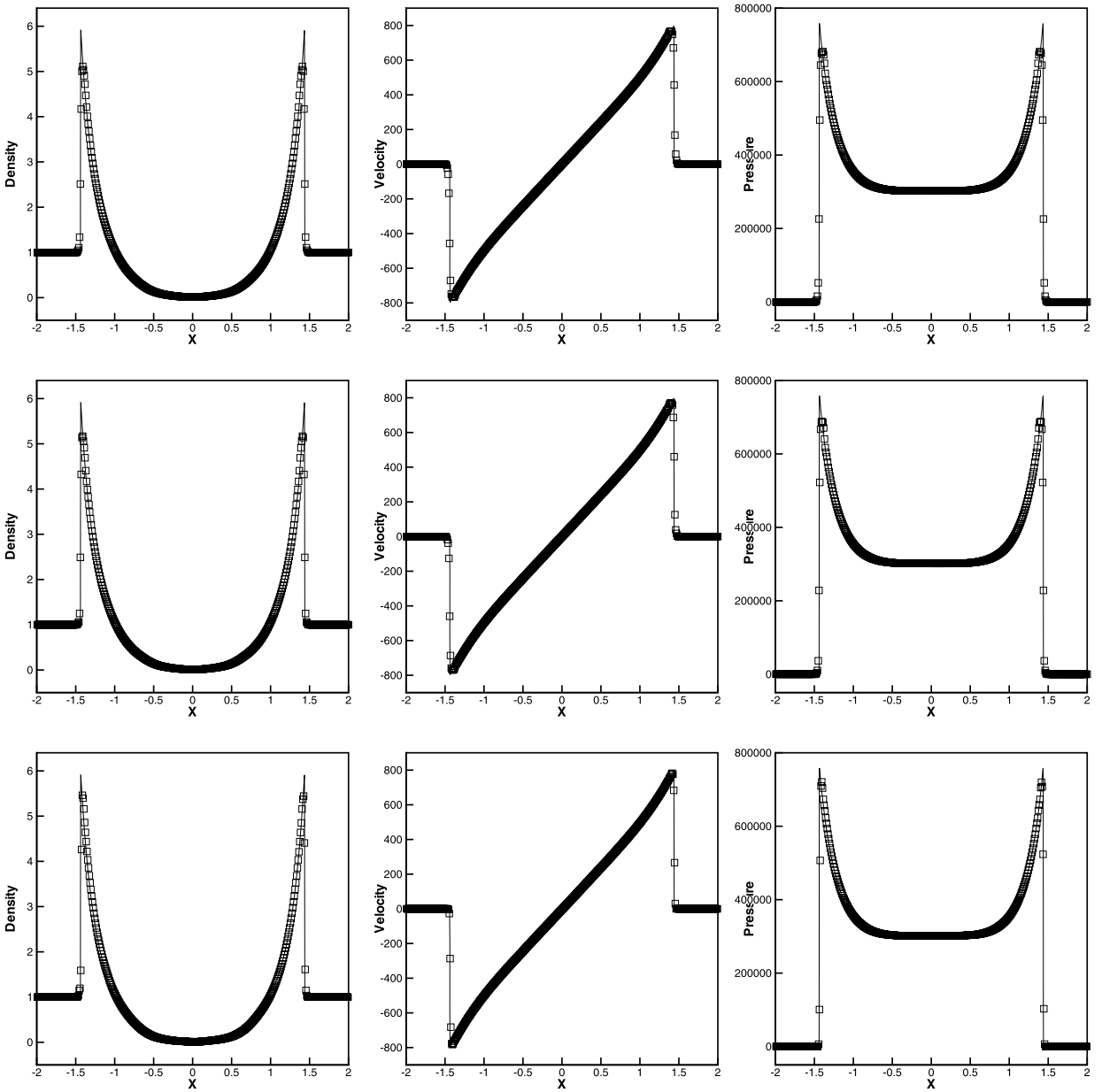

Fig. 4.4. The Sedov blast wave problem. $T = 0.001$. From left to right: density; velocity; pressure. From top to bottom: WENO5-FD, WENO7-FD, and WENO9-FD. Solid line: the exact solution; squares: the results of WENO schemes. Grid points: 400.

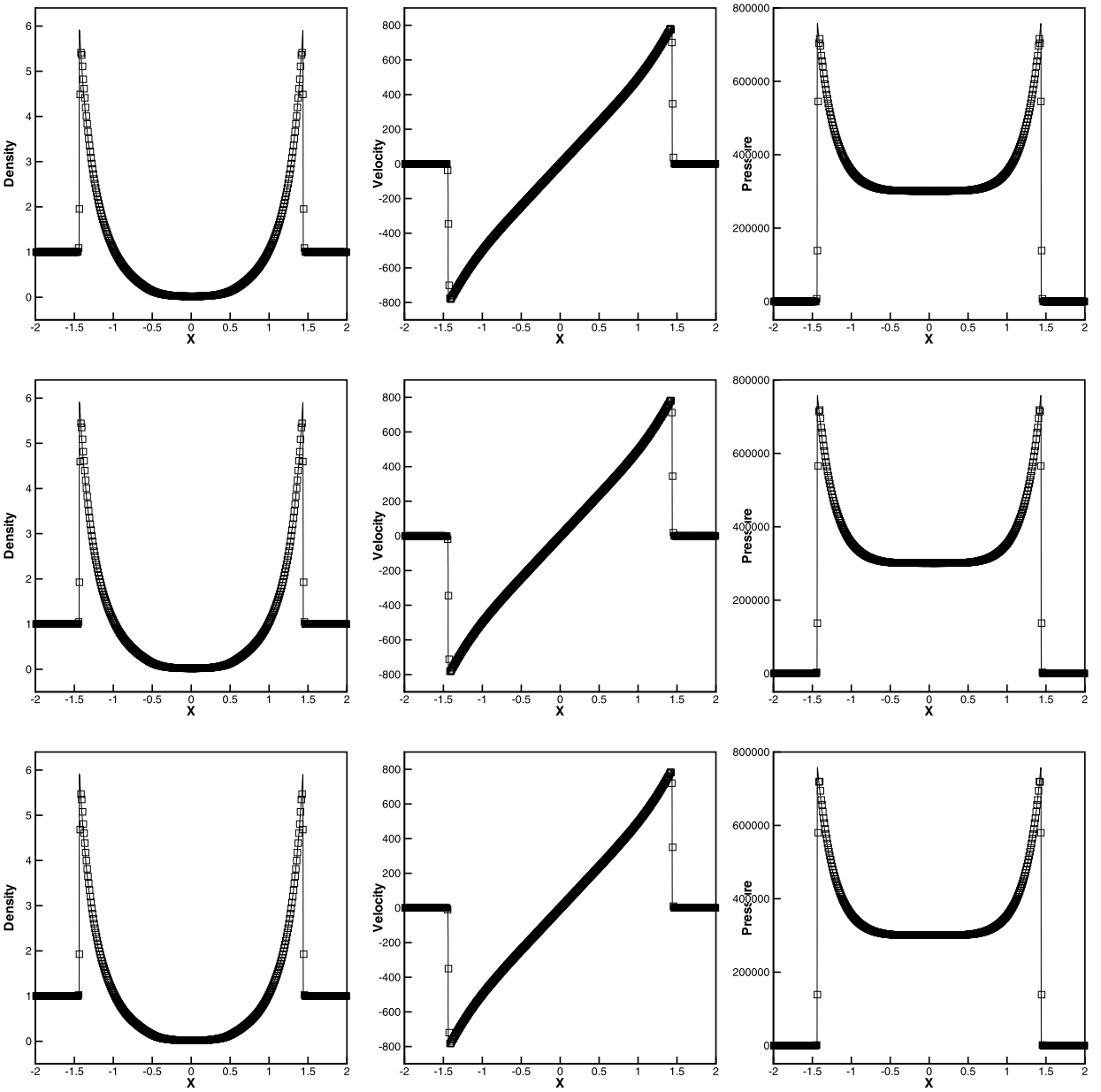

Fig. 4.5. The Sedov blast wave problem. $T = 0.001$. From left to right: density; velocity; pressure. From top to bottom: WENO5-FV, WENO7-FV, and WENO9-FV. Solid line: the exact solution; squares: the results of WENO schemes. Grid cells: 400.

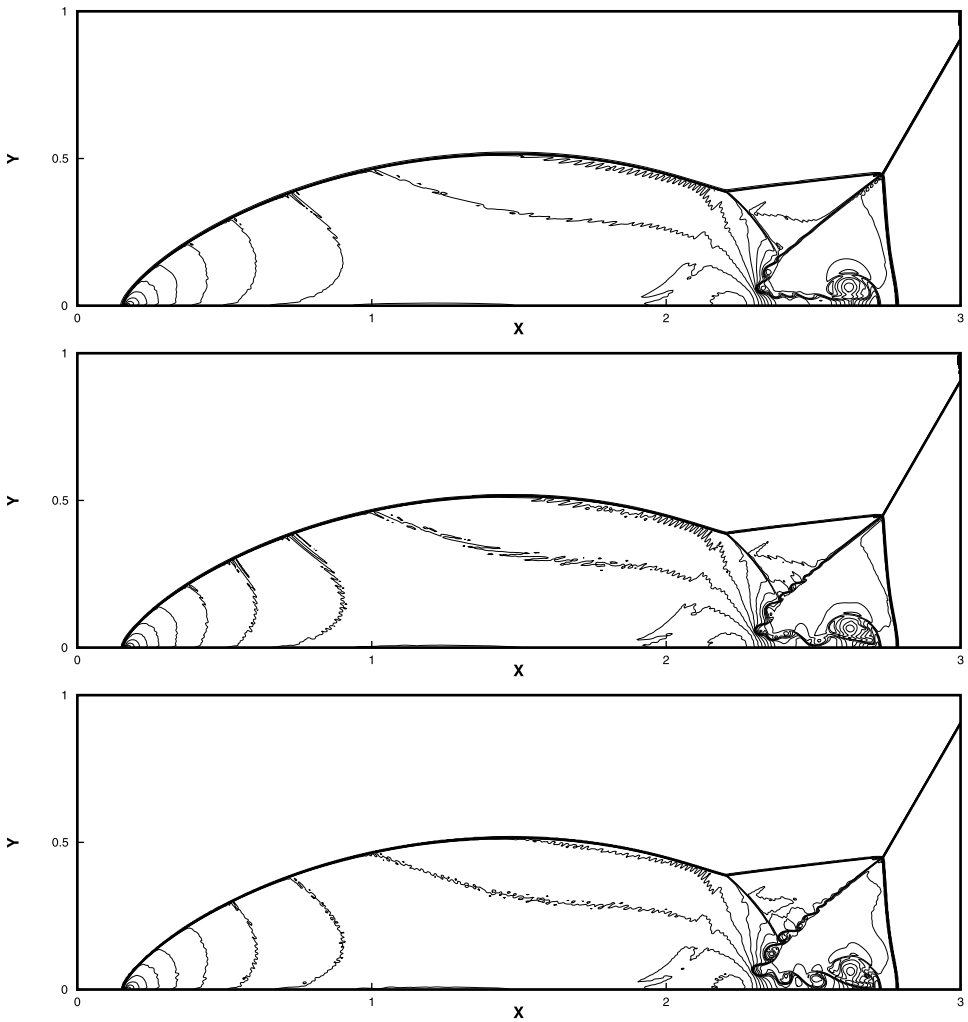

Fig. 4.6. Double Mach reflection problem. $T = 0.2$. 30 equally spaced density contours from 1.5 to 22.7. From top to bottom: WENO5-FD, WENO7-FD, and WENO9-FD. Grid points: 1200×400 in the region of $[0, 3] \times [0, 1]$.

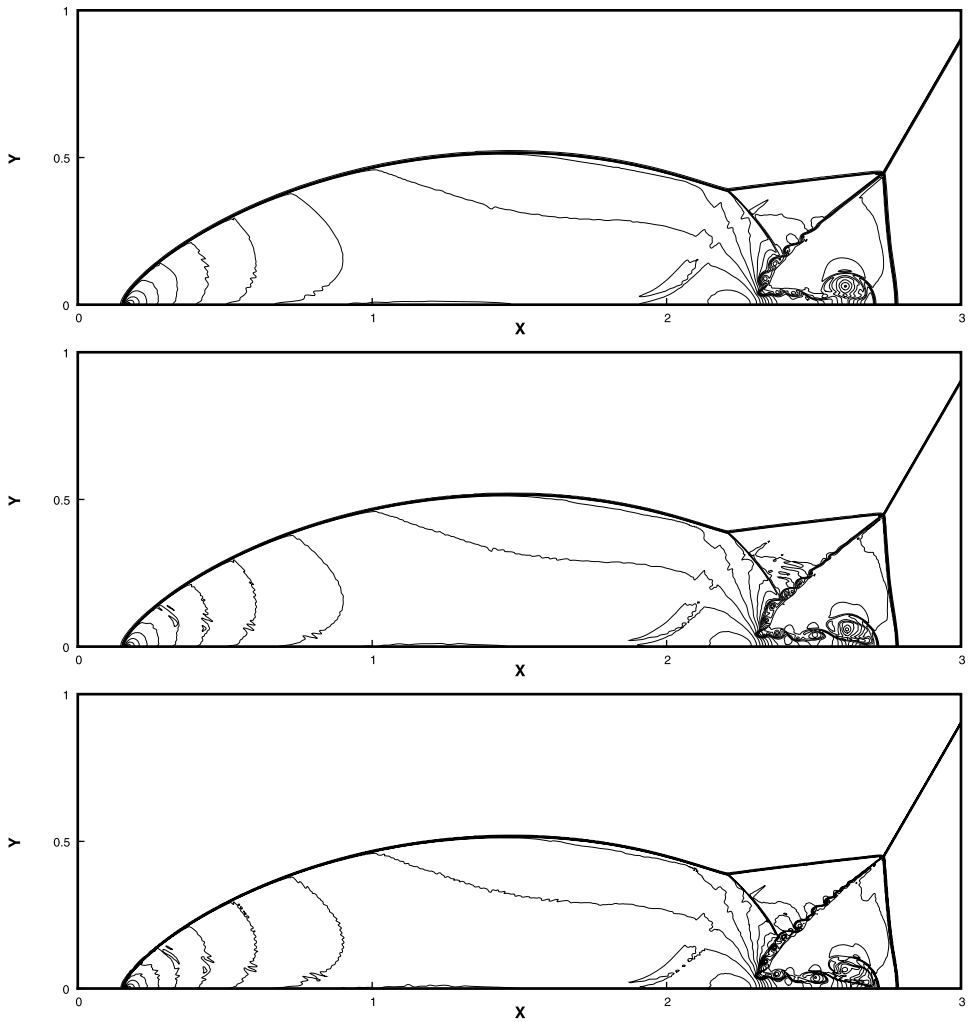

Fig. 4.7. Double Mach reflection problem. $T = 0.2$. 30 equally spaced density contours from 1.5 to 22.7. From top to bottom: WENO5-FV, WENO7-FV, and WENO9-FV. Grid cells: 1200×400 in the region of $[0, 3] \times [0, 1]$.

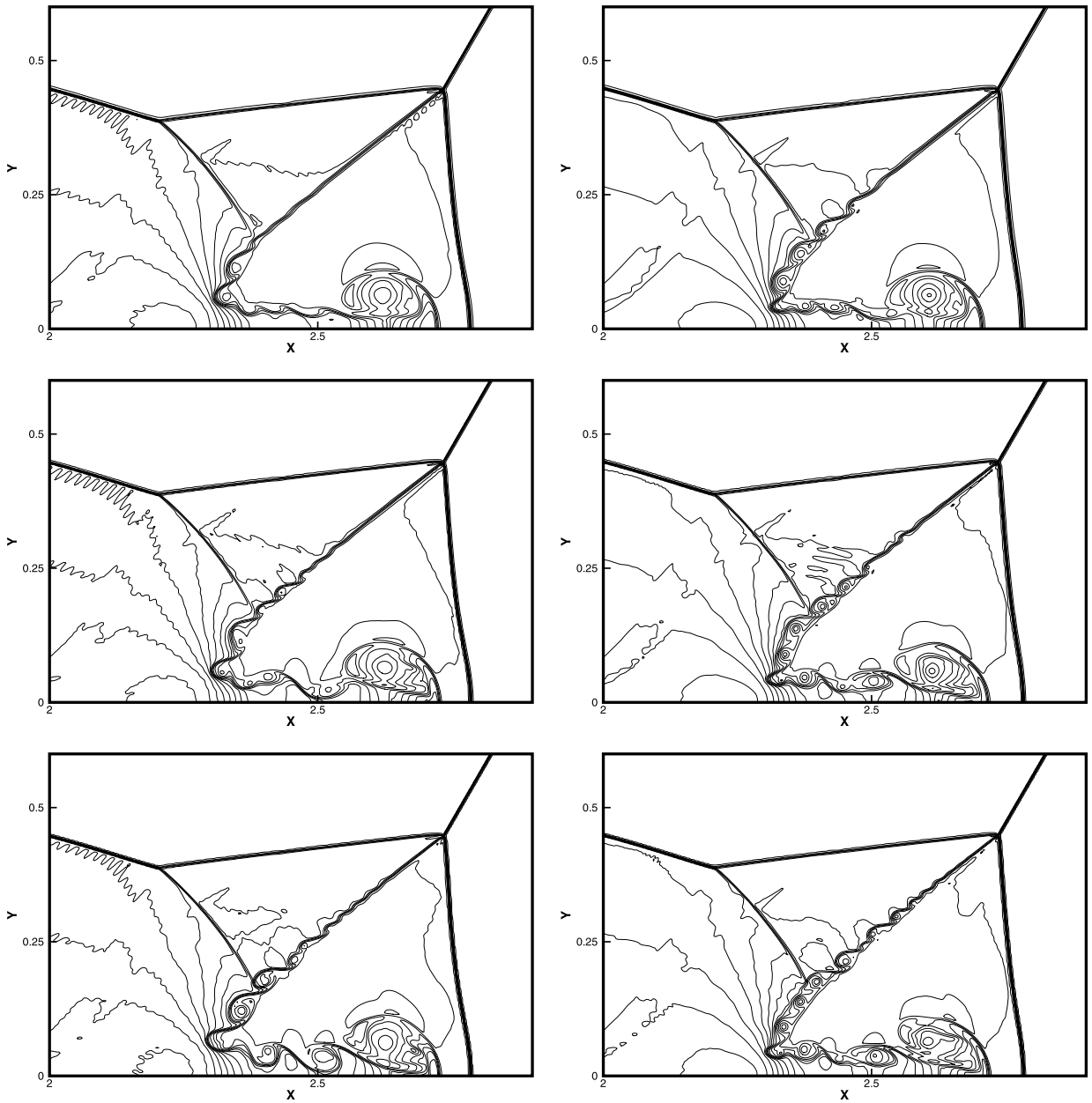

Fig. 4.8. Double Mach reflection problem. $T = 0.2$. 30 equally spaced density contours from 1.5 to 22.7, zoom-in pictures around the Mach stem (bottom). From left to right: WENO-FD and WENO-FV. From top to bottom: WENO5, WENO7, and WENO9. Grid points/cells: 1200×400 in the region of $[0, 3] \times [0, 1]$.

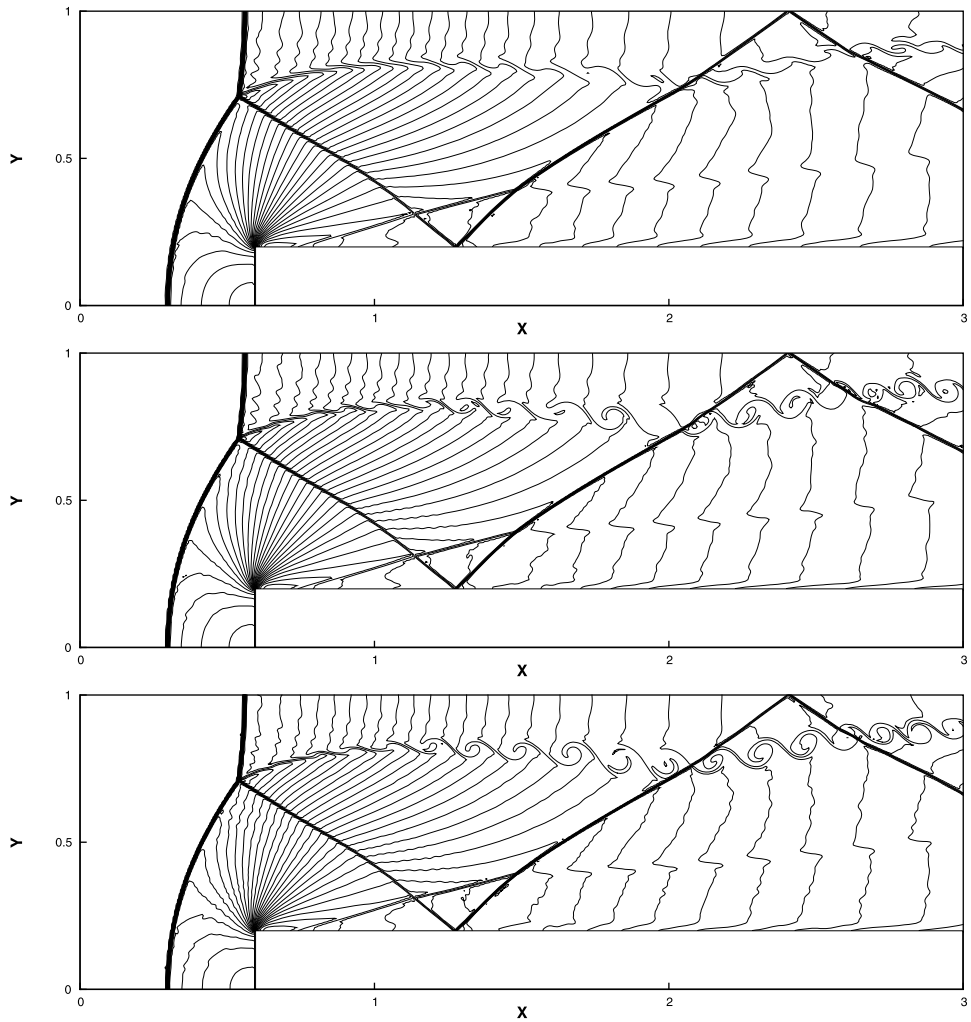

Fig. 4.9. Forward step problem. $T = 4.0$. 30 equally spaced density contours from 0.32 to 6.15. From top to bottom: WENO5-FD, WENO7-FD, and WENO9-FD. Grid points: 600×200.

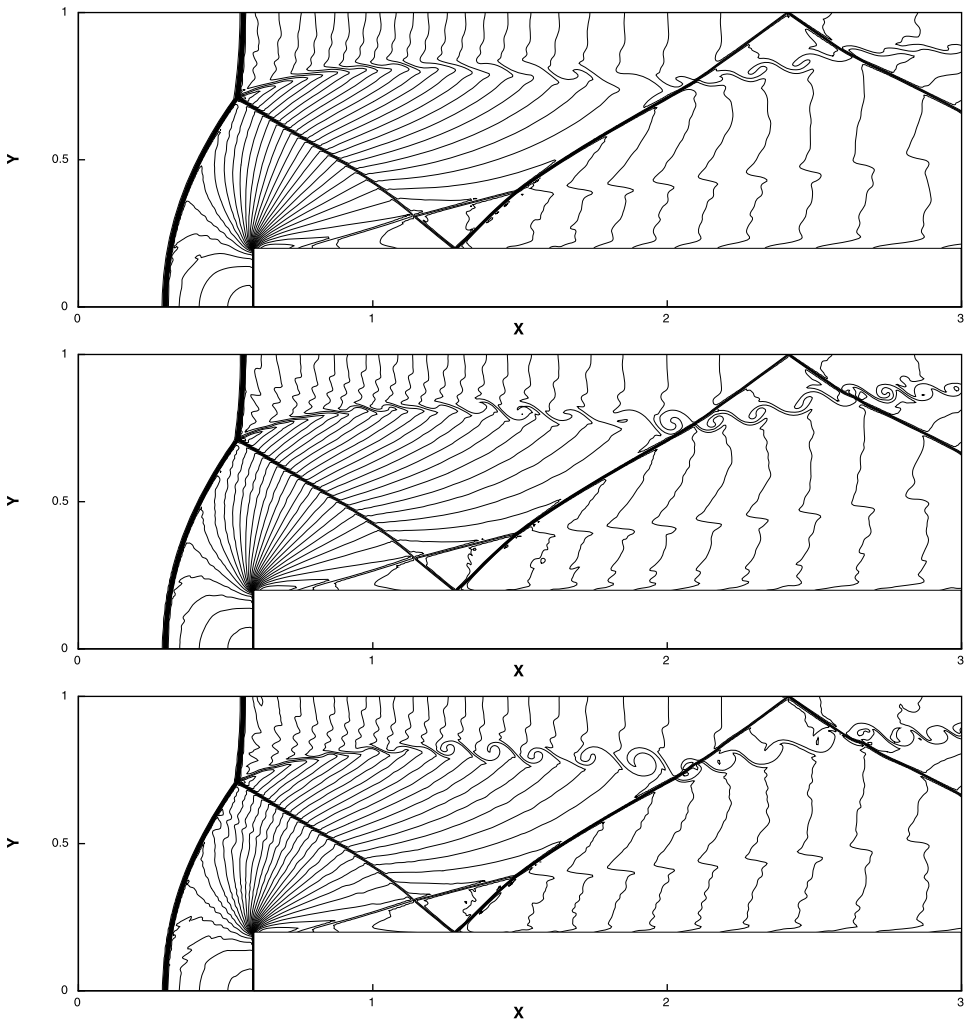

Fig. 4.10. Forward step problem. $T = 4.0$. 30 equally spaced density contours from 0.32 to 6.15. From top to bottom: WENO5-FV, WENO7-FV, and WENO9-FV. Grid cells: 600×200.

References

[1] D.S. Balsara, S. Garain, C.-W. Shu, An efficient class of WENO schemes with adaptive order, J. Comput. Phys. 326 (2016) 780–804.
[2] D.S. Balsara, C.-W. Shu, Monotonicity preserving weighted essentially non-oscillatory schemes with increasingly high order of accuracy, J. Comput. Phys. 160 (2000) 405–452.
[3] R. Borges, M. Carmona, B. Costa, W.S. Don, An improved weighted essentially non-oscillatory scheme for hyperbolic conservation laws, J. Comput. Phys. 227 (2008) 3191–3211.
[4] R. Bürger, A. Kozakevicius, Adaptive multiresolution WENO schemes for multi-species kinematic flow models, J. Comput. Phys. 224 (2007) 1190–1222.
[5] G. Capdeville, A central WENO scheme for solving hyperbolic conservation laws on non-uniform meshes, J. Comput. Phys. 227 (2008) 2977–3014.
[6] J. Casper, Finite-volume implementation of high-order essentially nonoscillatory schemes in two dimensions, AIAA J. 30 (1992) 2829–2835.
[7] J. Casper, H.L. Atkins, A finite-volume high-order ENO scheme for two-dimensional hyperbolic systems, J. Comput. Phys. 106 (1993) 62–76.
[8] M. Castro, B. Costa, W.S. Don, High order weighted essentially non-oscillatory WENO-Z schemes for hyperbolic conservation laws, J. Comput. Phys. 230 (2011) 1766–1792.
[9] G. Chiavassa, R. Donat, S. Müller, Multiresolution-based adaptive schemes for hyperbolic conservation laws, in: T. Plewa, T. Linde, V.G. Weiss (Eds.), Adaptive Mesh Refinement-Theory and Applications, in: Lecture Notes in Computational Science and Engineering, vol. 41, Springer-Verlag, Berlin, 2003, pp. 137–159.
[10] I. Cravero, M. Semplice, On the accuracy of WENO and CWENO reconstructions of third order on nonuniform meshes, J. Sci. Comput. 67 (2016) 1219–1246.
[11] W. Dahmen, B. Gottschlich-Müller, S. Müller, Multiresolution schemes for conservation laws, Numer. Math. 88 (2001) 399–443.
[12] M. Dumbser, M. Käser, Arbitrary high order non-oscillatory finite volume schemes on unstructured meshes for linear hyperbolic systems, J. Comput. Phys. 221 (2007) 693–723.
[13] L. Fu, X.Y.Y. Hu, N.A. Adams, A family of high-order targeted ENO schemes for compressible-fluid simulations, J. Comput. Phys. 305 (2016) 333–359.
[14] A. Harten, High resolution schemes for hyperbolic conservation laws, J. Comput. Phys. 49 (3) (1983) 357–393.
[15] A. Harten, Preliminary results on the extension of ENO schemes to two-dimensional problems, in: C. Carasso, et al. (Eds.), Proceedings, International Conference on Nonlinear Hyperbolic Problems, Saint-Etienne, 1987, in: Lecture Notes in Mathematics, Springer-Verlag, Berlin, 1986.

[16] A. Harten, Multi-Resolution Analysis for ENO Schemes, Contract No. NAS1-18605, Institute for Computer Applications in Science and Engineering, NASA Langley Research Center, Hampton, Virginia 23665-5225, September 1991.
[17] A. Harten, Discrete multi-resolution analysis and generalized wavelets, Appl. Numer. Math. 12 (1993) 153–192.
[18] A. Harten, Adaptive multiresolution schemes for shock computations, Comput. Phys. 115 (1994) 319–338.
[19] A. Harten, Multiresolution algorithms for the numerical solution of hyperbolic conservation laws, Commun. Pure Appl. Math. 48 (1995) 1305–1342.
[20] A. Harten, Multiresolution representation of data: a general framework, SIAM J. Numer. Anal. 33 (1996) 1205–1256.
[21] A. Harten, B. Engquist, S. Osher, S. Chakravarthy, Uniformly high order accurate essentially non-oscillatory schemes III, J. Comput. Phys. 71 (1987) 231–323.
[22] A. Harten, S. Osher, Uniformly High-order Accurate Non-oscillatory Schemes, IMRC Technical Summary Rept. 2823, Univ. of Wisconsin, Madison, WI, May 1985.
[23] G. Hu, R. Li, T. Tang, A robust WENO type finite volume solver for steady Euler equations on unstructured grids, Commun. Comput. Phys. 9 (2011) 627–648.
[24] C. Hu, C.-W. Shu, Weighted essentially non-oscillatory schemes on triangular meshes, J. Comput. Phys. 150 (1999) 97–127.
[25] G.-S. Jiang, C.-W. Shu, Efficient implementation of weighted ENO schemes, J. Comput. Phys. 126 (1996) 202–228.
[26] O. Kolb, On the full and global accuracy of a compact third order WENO scheme, SIAM J. Numer. Anal. 52 (5) (2014) 2335–2355.
[27] V.P. Korobeinikov, Problems of Point-Blast Theory, American Institute of Physics, 1991.
[28] D. Levy, G. Puppo, G. Russo, Central WENO schemes for hyperbolic systems of conservation laws M2AN, Math. Model. Numer. Anal. 33 (1999) 547–571.
[29] D. Levy, G. Puppo, G. Russo, Compact central WENO schemes for multidimensional conservation laws, SIAM J. Sci. Comput. 22 (2) (2000) 656–672.
[30] X.D. Liu, S. Osher, T. Chan, Weighted essentially non-oscillatory schemes, J. Comput. Phys. 115 (1994) 200–212.
[31] Y.J. Liu, Central schemes on overlapping cells, J. Comput. Phys. 209 (2005) 82–104.
[32] Y.J. Liu, C.-W. Shu, E. Tadmor, M.P. Zhang, Central discontinuous Galerkin methods on overlapping cells with a nonoscillatory hierarchical reconstruction, SIAM J. Numer. Anal. 45 (2007) 2442–2467.
[33] Y.J. Liu, C.-W. Shu, E. Tadmor, M.P. Zhang, Non-oscillatory hierarchical reconstruction for central and finite volume schemes, Commun. Comput. Phys. 2 (2007) 933–963.
[34] Y.J. Liu, C.-W. Shu, E. Tadmor, M.P. Zhang, L^2 stability analysis of the central discontinuous Galerkin method and a comparison between the central and regular discontinuous Galerkin methods, ESAIM M2AN 42 (2008) 593–607.
[35] Y.J. Liu, C.-W. Shu, E. Tadmor, M.P. Zhang, Central local discontinuous Galerkin methods on overlapping cells for diffusion equations, ESAIM M2AN 45 (2011) 1009–1032.
[36] Y.J. Liu, C.-W. Shu, Z.L. Xu, Hierarchical reconstruction with up to second degree remainder for solving nonlinear conservation laws, Nonlinearity 22 (2009) 2799–2812.
[37] Y. Liu, Y.T. Zhang, A robust reconstruction for unstructured WENO schemes, J. Sci. Comput. 54 (2013) 603–621.
[38] S. Pirozzoli, Conservative hybrid compact-WENO schemes for shock–turbulence interaction, J. Comput. Phys. 178 (2002) 81–117.
[39] L.I. Sedov, Similarity and Dimensional Methods in Mechanics, Academic Press, New York, 1959.
[40] M. Semplice, A. Coco, G. Russo, Adaptive mesh refinement for hyperbolic systems based on third-order compact WENO reconstruction, J. Sci. Comput. 66 (2016) 692–724.
[41] Y.Q. Shen, G.W. Yang, Hybrid finite compact-WENO schemes for shock calculation, Int. J. Numer. Methods Fluids 53 (2007) 531–560.
[42] Y.Q. Shen, G.C. Zha, A robust seventh-order WENO scheme and its applications, in: 46th AIAA Aerospace Sciences Meeting and Exhibit, Reno, Nevada, 2008, AIAA 2008-757.
[43] J. Shi, C.Q. Hu, C.-W. Shu, A technique of treating negative weights in WENO schemes, J. Comput. Phys. 175 (2002) 108–127.
[44] C.-W. Shu, Essentially non-oscillatory and weighted essentially non-oscillatory schemes for hyperbolic conservation laws, in: B. Cockburn, C. Johnson, C.-W. Shu, E. Tadmor, A. Quarteroni (Eds.), Advanced Numerical Approximation of Nonlinear Hyperbolic Equations, in: Lecture Notes in Mathematics, vol. 1697, Springer, Berlin, 1998, pp. 325–432.
[45] C.-W. Shu, High order weighted essentially non-oscillatory schemes for convection dominated problems, SIAM Rev. 51 (2009) 82–126.
[46] C.-W. Shu, S. Osher, Efficient implementation of essentially non-oscillatory shock capturing schemes, J. Comput. Phys. 77 (1988) 439–471.
[47] C.-W. Shu, S. Osher, Efficient implementation of essentially non-oscillatory shock capturing schemes, II, J. Comput. Phys. 83 (1989) 32–78.
[48] Z.J. Wang, R.F. Chen, Optimized weighted essentially non-oscillatory schemes for linear waves with discontinuity, J. Comput. Phys. 174 (2001) 381–404.
[49] P. Woodward, P. Colella, The numerical simulation of two-dimensional fluid flow with strong shocks, J. Comput. Phys. 54 (1984) 115–173.
[50] T. Xiong, J.-M. Qiu, Z. Xu, Parameterized positive preserving flux limiters for the high order finite difference WENO scheme solving compressible Euler equations, J. Sci. Comput. 67 (2016) 1066–1088.
[51] Z.L. Xu, Y.J. Liu, H.J. Du, G. Lin, C.-W. Shu, Point-wise hierarchical reconstruction for discontinuous Galerkin and finite volume methods for solving conservation laws, J. Comput. Phys. 230 (2011) 6843–6865.
[52] Z.L. Xu, Y.J. Liu, C.-W. Shu, Hierarchical reconstruction for discontinuous Galerkin methods on unstructured grids with a WENO type linear reconstruction and partial neighboring cells, J. Comput. Phys. 228 (2009) 2194–2212.
[53] X. Zhang, C.-W. Shu, On maximum-principle-satisfying high order schemes for scalar conservation laws, J. Comput. Phys. 229 (2010) 3091–3120.
[54] X. Zhang, C.-W. Shu, On positivity preserving high order discontinuous Galerkin schemes for compressible Euler equations on rectangular meshes, J. Comput. Phys. 229 (2010) 8918–8934.
[55] X. Zhang, C.-W. Shu, Maximum-principle-satisfying and positivity-preserving high order schemes for conservation laws: survey and new developments, Proc. R. Soc. A 467 (2011) 2752–2776.
[56] X. Zhang, C.-W. Shu, Positivity-preserving high order finite difference WENO schemes for compressible Euler equations, J. Comput. Phys. 231 (2012) 2245–2258.
[57] Y.T. Zhang, C.-W. Shu, High order WENO schemes for Hamilton–Jacobi equations on triangular meshes, SIAM J. Sci. Comput. 24 (2003) 1005–1030.
[58] Y.T. Zhang, C.-W. Shu, Third order WENO scheme on three dimensional tetrahedral meshes, Commun. Comput. Phys. 5 (2009) 836–848.
[59] X. Zhong, C.-W. Shu, A simple weighted essentially nonoscillatory limiter for Runge–Kutta discontinuous Galerkin methods, J. Comput. Phys. 232 (2013) 397–415.
[60] J. Zhu, J. Qiu, A new fifth order finite difference WENO scheme for solving hyperbolic conservation laws, J. Comput. Phys. 318 (2016) 110–121.
[61] J. Zhu, J. Qiu, A new type of finite volume WENO schemes for hyperbolic conservation laws, J. Sci. Comput. 73 (2017) 1338–1359.
[62] J. Zhu, X. Zhong, C.-W. Shu, J. Qiu, Runge–Kutta discontinuous Galerkin method using a new type of WENO limiters on unstructured meshes, J. Comput. Phys. 248 (2013) 200–220.